Hybrid Perovskites; New Opportunities beyond Oxides

Wei Li[1,2*], Zheming Wang[3], Felix Deschler[4], Song Gao[3*], Richard H. Friend[4*],

Anthony K. Cheetham[5*]

[1]*School of Physics, Huazhong University of Science and Technology, Wuhan 430074, China*

[2]*Laboratory for Optical Information Technology, Wuhan Institute of Technology, Wuhan 430205, China*

[3]*College of Chemistry and Molecular Engineering, Peking University, Beijing 100871, China*

[4]*Cavendish Laboratory, University of Cambridge, JJ Thomson Avenue, Cambridge CB3 0HE, UK*

[5]*Department of Materials Science and Metallurgy, University of Cambridge, Charles Babbage Road, Cambridge CB3 0FS, UK*

Abstract | Current studies on hybrid organic-inorganic perovskites (HOIPs) are predominantly focused on hybrid halides for photovoltaic and optoelectronic properties. However, the field of HOIPs is a much broader one that encompasses other important families, such as formates, azides, dicyanamides, cyanides and dicyanometallates. These HOIP materials have several common features, including not only the ABX_3 structural architecture but also the presence of organic ammonium cations and their associated physical properties. These features lead to some remarkable behaviour, especially in the domain of phase transitions. In this review, we summarise the recent advances in the synthesis, structures and physical properties of all HOIP classes and discuss future opportunities in this exciting area.

The word perovskite was coined to name the calcium titanium oxide mineral, $CaTiO_3$, which was discovered in the Ural Mountains of Russia by the German mineralogist Gustav Rose and named in honour of the Russian Count, Lev A. Perovski[1]. Nowadays, perovskite refers to a broad class of materials which have the same type of structure as $CaTiO_3$, known as the perovskite structure[2]. The general chemical formula

for perovskite materials is ABX_3, where A and B are two cations with distinct sizes, and X is an anion that coordinates to B. The A atoms are normally larger than the B atoms, and the B cation is six-coordinated by the X-site anion to form a BX_6 octahedron. Then, these octahedra are corner-shared to form a three-dimensional framework where the A-site cations are located in the framework cavities (Figure 1a).

Hybrid organic-inorganic perovskites (HOIPs) are a more recent class of ABX_3 materials in which the A- and/or X-sites are replaced by the organic ammonium cations and/or organic linkers, respectively (hybrid layered and hexagonal perovskites are not

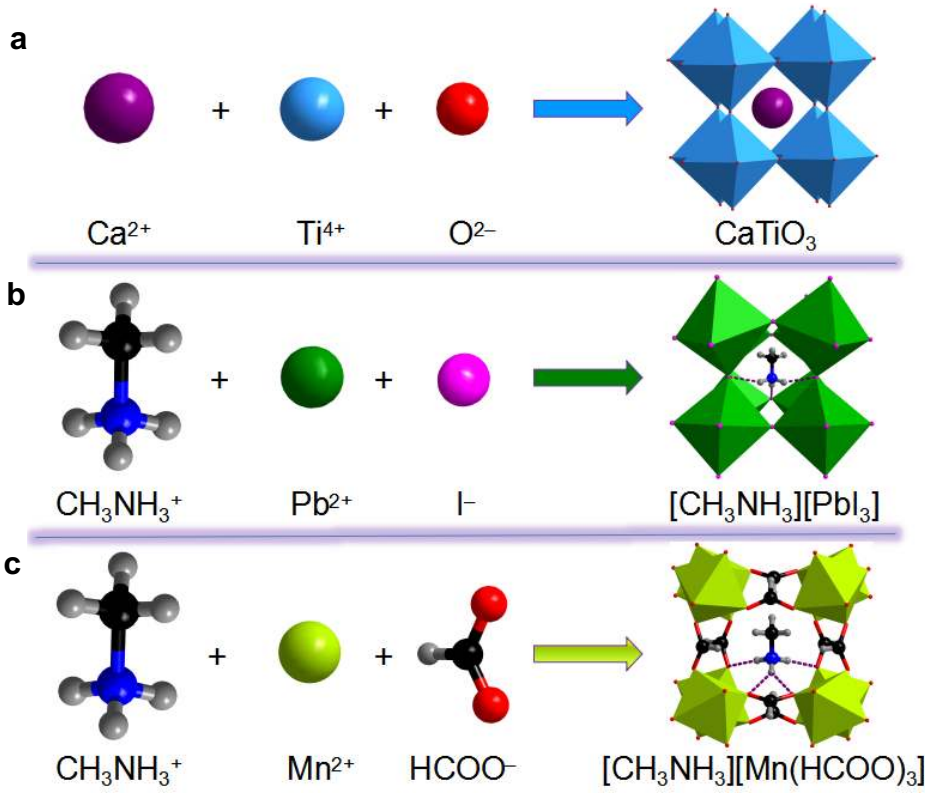

Figure 1 | **Evolution from perovskite oxides to HOIPs with organic A-site, then to HOIPs with both organic A- and X-sites (Metal-organic framework perovskites).** a | $CaTiO_3$ (Orthorhombic, *Pbnm*, REF. [3]). b | [MA][PbI_3] (Orthorhombic, *Pnma*, REF. [4]). c | [MA][$Mn(HCOO)_3$] (Orthorhombic, *Pnma*, REF. [5]). Colour scheme: Ca, violet; Ti, turquoise; Pb, green; Mn, lime; I, pink; O, red; N, blue; C, black; H, light grey. Hydrogen bonds are denoted as dotted purple lines.

discussed herein due to length limitations). The organic components in the structure of these HOIPs give additional functionalities and structural flexibility that cannot be achieved in purely inorganic perovskites. Most importantly, their diverse structural and chemical variability offer substantial opportunities for tuning and modulating their physical properties *via* facile chemical modification[6]. The discovery of hybrid perovskites was first reported by Weber in a paper that described the cubic perovskite structure of $(MA)PbX_3$ (MA = methylammonium and X = Cl, Br, I) (Figure 1b) in 1978[9]. By extending the X-site from a single halide to bitopic molecular linkers, such as azide (N_3^-), cyanide (CN^-) and boronhydride (BH_4^-), several other families of HOIPs were formed[5, 10, 11]. The introduction of additional organic components into the X-site gives another variety of HOIP derivatives, namely metal-organic framework perovskites (Figure 1c).

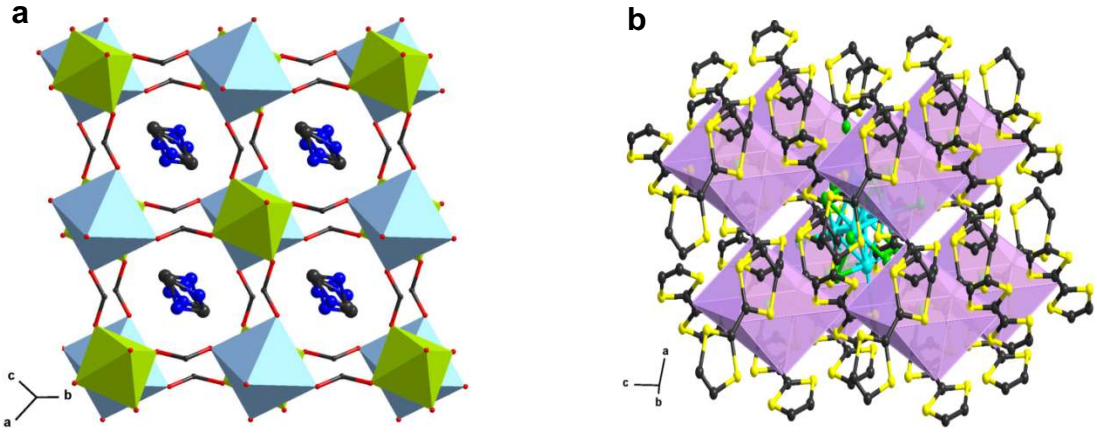

Figure 2 | **HOIPs with double perovskite and antiperovskite structures.** a | $[DMA]_2[NaFe(HCOO)_6]$ (REF. [7]). b | $(TTF^{\bullet})_3[Cl(Mo_6Cl_{14})]$ (REF. [8]). Colour scheme: Na, chartreuse; Fe, light cyan; Mo, cyan; S, yellow; Cl, green; O, red; N, blue; C, black. The DMA cation is equally disordered at three positions in the double perovskite; the light magenta octahedra are constructed by the central Cl atom and six neighbouring $TTF^{\bullet+}$ cations. Hydrogen atoms and hydrogen bonds are omitted for clarity.

Metal–formate and metal–dicyanamide perovskites are well known examples, in which

the A- and X-sites are organic ammonium cations and $HCOO^-/N(CN)_2^-$ linkers, respectively[12, 13].

Like conventional perovskites, HOIPs can also be categorised as ABX_3 perovskites, $A_2BB'X_6$ double perovskites and A_3BX antiperovskite subclasses from a broader viewpoint of structure. Double hybrid perovskites have been extensively exemplified *via* replacing the divalent metals by mixed monovalent and trivalent ones in the azide[14], cyanide[5, 15, 16] and formate[7, 17] HOIPs. However, the hybrid antiperovskites are still very rare, and the only known examples are the ternary tetrathiafulvalenium salts, $(TTF^{\bullet})_3[(X)(Mo_6X_{14})]$ ($TTF^{\bullet+}$ = tetrathiafulvalenium; X = C1, Br, I), which were prepared in 1991[8].

The abundant variations of organic components and metal salts offer enormous chemical possibilities for creating HOIPs, and the known HOIPs now span a significant part of the periodic table, much like their oxide counterparts. The crystal structures of HOIPs follow the Goldschmidt tolerance factors (TFs) to indicate the ionic size mismatches that the perovskite architecture can tolerate[18]. As the A-site and/or X-site in the HOIPs are replaced by the molecular building blocks, the TFs can be adapted to the following equation:

$$t = (r_{Aeff} + r_{Xeff})/\sqrt{2}(r_B + 0.5\ h_{Xeff})$$

where r_B defines the Shannon ionic radius of the B-site metal, and r_{Aeff}, r_{Xeff} and h_{Xeff} denote the effective radius of the A-site, and the effective radius and length of the X-site molecular ions, respectively[19]. By tabulating most possible A-site, B-site and X-site combinations in HOIPs, a significant number of TFs are found to lie in the range of ~0.8-1.0 (Table 1)[20]. Such results are reminiscent with those in conventional perovskites, and

Table 1 | Summary of the chemical variabilities, structural diversities and physical properties of HOIPs

HOIPs	A-site	B-site	X-site	Symmetry	TFs	Physical properties
Halides	MA, FA	Pb^{2+}, Sn^{2+}, Ge^{2+}	Cl^-, Br^-, I^-	Orthorhombic Trigonal Tetragonal Cubic	~0.912-1.142	Semiconductivity Photovoltaics Laser physics Light-emitting diodes Mechanical properties
	MA	$^{\S}K^+/Bi^{3+}$, Tl^+/Bi^{3+}			~0.906-923[#]	
	[‡]PIP, DABCO	K^+, Cs^+, Rb^+	Cl^-	Monoclinic Orthorhombic Trigonal	~0.922-1.037	
Formates	Cs^+, K^+, NH_4^+, MA, FA, GUA, EA, DMA, AZE, HIM, HAZ	Mg^{2+}, Mn^{2+}, Fe^{2+}, Co^{2+}, Ni^{2+}, Cu^{2+}, Zn^{2+}, Cd^{2+}	$HCOO^-$	Monoclinic Orthorhombic Trigonal Tetragonal	~0.784-1.001*	Magnetism Dielectricity Ferroelectricity Ferroelasticity Multiferroicity Mechanical properties
	TrMA, DMA, EA	$^{\S}Na^+/Cr^{3+}$, Na^+/Al^{3+}, Na^+/Fe^{3+}, K^+/Sc^{3+}	$HCOO^-$	Triclinic Trigonal	~0.897-1.040[#]	
Azides	MA, DMA, TrMA, TMA,	Mn^{2+}, Cd^{2+}, Ca^{2+}	N_3^-	Triclinic Monoclinic Cubic	~0.786-1.023	Magnetism Dielectricity Ferroelasticity
	TMA	$^{\S}Na^+/Cr^{3+}$, Na^+/Fe^{3+}, K^+/Fe^{3+}, K^+/Cr^{3+}			~0.934-1.008[#]	
Dicyanamides	[$]BPEA, BPTA, SPh_3, TPrA	Mn^{2+}, Co^{2+}, Ni^{2+}	$[N(CN)_2]^-$	Orthorhombic Tetragonal	~1.142-1.166	Magnetism Dielectricity
Dicyanometallates	PPN	Cd^{2+}	$[Ag(CN)_2]^-$	Monoclinic Trigonal Cubic	~1.033-1.141[$]	Magnetism
		Mn^{2+}, Co^{2+}, Ni^{2+}, Cd^{2+}	$[Au(CN)_2]^-$			
Cyanides	HIM, DMA, MA, TMA, TrMA, GUA	$^{\S}K^+/Fe^{3+}$, K^+/Co^{3+}	CN^-	Triclinic Monoclinic Cubic	~0.840-1.031[#]	Dielectricity
Boronhydrides	MA	Ca^{2+}	[¶]BH_4^-	Cubic	~0.980	Hydrogen storage

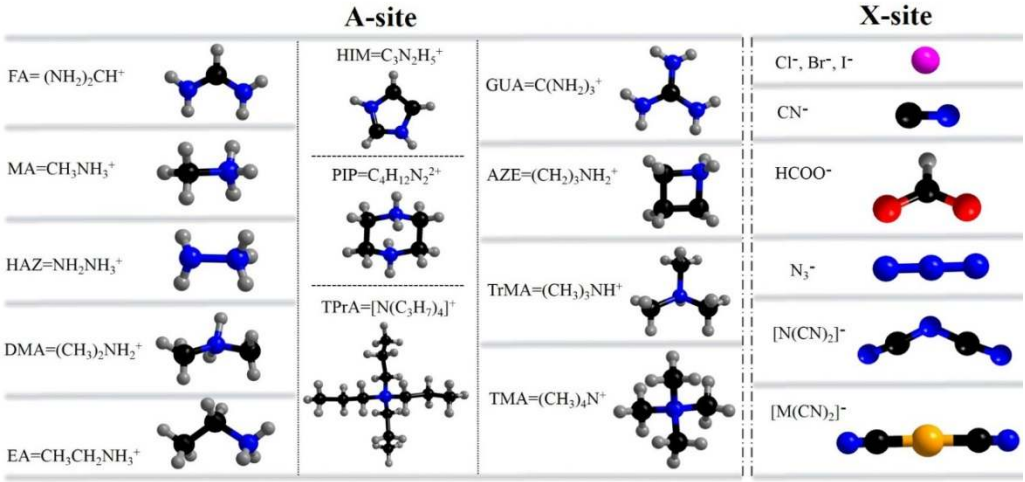

HOIPs, hybrid organic-inorganic perovskites. TFs, tolerance factors. [$]Mixed B-sites in hybrid double perovskites. [‡][PIP][KCl_3], [PIP][$CsCl_3$], [PIP][$RbCl_3$], [DABCO][$RbCl_3$] and [DABCO][$CsCl_3$] are not discussed in the halide HOIPs as they are not solar cell metal-halide perovskites (REF. [21]). *The unique TFs of $KCo(HCOO)_3$ (REF. [22]), $CsCo(HCOO)_3$ (REF. [23]) and $[NH_4][Cd(HCOO)_3]$ (REF. [24]) which lie in the range ~0.620-0.700 are not presented in the table due to the special *anti-syn* coordination mode of the formate linker. [#]The TFs of hybrid double perovskites, $A_2BB'X_6$, were calculated using the adapted formula $t = (r_{Aeff} + r_{Xeff})/\sqrt{2}(r_B/2 + r_B/2 + 0.5\ h_{Xeff})$. $r_{Aeff} = r_{mass} + r_{ion}$, where r_{mass} is defined as the distance between the centre of the mass of the A-site organic molecule ion and the atom with the largest distance to the centre of mass (excluding hydrogen atoms), and r_{ion} is the corresponding ionic radius of the aforementioned atom. r_{Xeff} can be defined in a similar way as r_{Aeff}. [$]Since the BPEA, BPTA and SPh_3 cations are larger than the pseudocubic cavity, the relevant TFs were not able to be calculated. [¶]The molecular structure of BH_4^- is not listed in the table because of the structural unavailability of $[MA][Ca(BH_4)_3]$. Colour scheme: oxygen, red; carbon, black; nitrogen, blue; hydrogen, light grey; halogen, purple.

demonstrate the extended validity of the Goldschmidt TFs and that the packing density plays a pivotal role in the formation of HOIPs. Moreover, this simple semi-empirical approach for assessing size compatibility can guide the rational design and synthesis of new HOIPs using compositions with desired functionalities. The recent discovery of some new formate and halide HOIPs has indeed validated this powerful tool for predicting experimental realisation[25, 26]. However, caution has been raised by Palgrave *et al.* as the TF metric shows limited suitability for predicting the stability of certain halides, and iodides in particular[27]. They modified the TF metric by considering the covalency of the B–X bonds (X = Cl, Br and I) when calculating the Shannon cation radii. In addition, they proposed another geometric factor, namely the octahedral factor (μ), which determines the fit of the B-site cation into the X_6 octahedon, to assess the compatibility of both the A- and B-site cations for the perovskite architecture. Employing a 2D t–μ structure mapping approach, the stability of nearly all hybrid perovskite halides has been successfully predicted.

The ideal perovskite structure adopts the cubic space group *Pm*-3*m* and has no variable parameters in the structure. By lowering the symmetry from this aristotype architecture, many perovskite structures with distortions can be obtained. This group-theoretical analysis has been used as a powerful tool to study the complex symmetry breaking and phase transitions of conventional perovskites[2 8]. In this approach, the displacements of the A- and B-sites, and the tilting of the BX_6 octahedral units, are the primary factors which lead to structural distortions[29, 30]. As the latter usually has a much greater effect on lattice parameters, it has been used to classify the allowed symmetry changes of perovskites[31-33]. For HOIPs in which the X-sites are composed of only one

Box 1 | **Representative phase transition mechanisms of two prototypical HOIPs.**

In contrast to the octahedral tilting and displacements that are responsible for phase transitions in conventional perovskites, the transitions in HOIPs can have additional driving forces. In Figure B1a, the transition in [TMA][$Mn(N_3)_3$] is driven by the synergistic association of the off-centre displacement of the TMA guests, the order−disorder processes of both the azide ligands and the TMA cations, and a change in the MnN_6 octahedral tilting (from Glazer notation $a^0a^0a^0$ to $a^+b^-c^+$) (REFs. [34, 35]). Notably, some adjacent octahedra in the low symmetry phase rotate along same direction, which is not possible in oxide analogues. In Figure B1b, the octahedral tilting of MnO_6 in [AZE][$Mn(HCOO)_3$] exhibits trivial changes across the ferroelastic transition (from $a^-b^+a^-$ to $a^-b^+c^-$), and the main driving force is the order-disorder of the A-site AZE cation and associated hydrogen bonding alterations (REF. [36]). This unique orthorhombic *Pnma* to monoclinic $P2_1/n$ transition, which is very uncommon in perovskite oxides, involves the X-point modes in the Brillouin zone in addition to the usual M- and R-point modes (as seen in oxides). These examples highlight the complex cooperation of the various driving forces during phase transitions in HOIPs. Colour scheme: Mn, green and yellow; O, red; N, blue; C, grey and black; H, light grey. The TMA and AZE cations are equally disordered at eight and three positions in the formate and azide HOIPs, respectively. Hydrogen atoms of the ethylene and methyl groups are omitted for clarity. Glazer notation describes the distorsion of BX_6 octahedra about the *a*, *b*, and *c* axes using symbols "+" and "–" to define whether the tilting between adjacent octahedra along a given axis is in-phase or out-of-phase (REF.[28]).

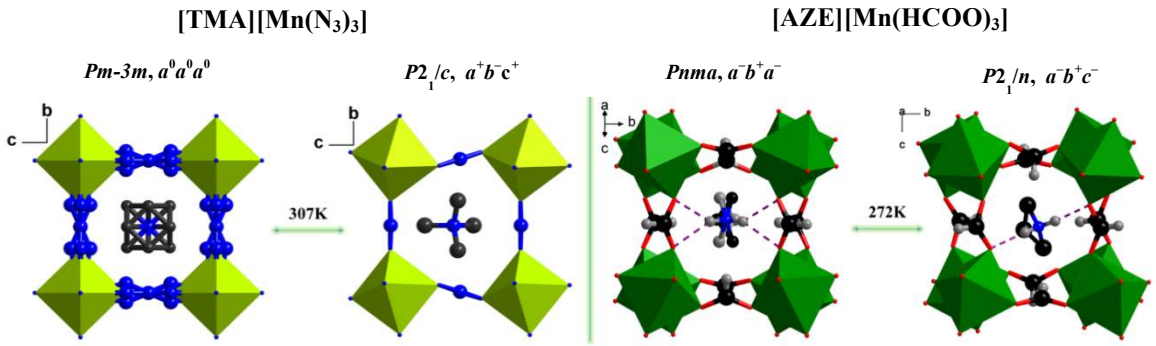

atom, such as in halides, it is apparent that their octahedral tiltings are similar to those in pure inorganics. Evolving the X-site from a single atom to a molecular linker seems to complicate the situation since the octahedra in the lattice are no longer corner-sharing.

However, the rigidity of most X-site ligands is strong enough to mediate the tilt from one octahedron to another, extending the validity of tilting analysis from inorganic perovskites to HOIPs. Inevitably, the much larger X-sites in HOIPs give rise to additional space for the octahedra to distort (Box 1). In certain situations, adjacent octahedra can even distort along the same orientation, adding new tilting possibilities that are inaccessible in oxides[34, 35] .

In addition to the octahedral tilting of the B-sites, the displacements of the A-sites and the dynamic motions of the A- and/or X-sites all need to be taken into account for the symmetry description of HOIPs. The displacements are in principle identical to those in inorganic perovskites, normally involving off-centre movements, though the situation is complicated due to the presence of organic cations rather than single atoms on the A-sites. The dynamic movement of the organic A-site (occasionally occurring also in the X-site) is defined as disorder, and switching from a disordered to an ordered state can induce symmetry changes. More interestingly, the order-disorder of the A-site organic cation inevitably changes the hydrogen-bonding and dispersion forces, which in turn can influence the symmetry variations (Box 1)[36]. Such synergistic combination of octahedral tilting, displacements and order-disorder often result in more complicated phase transitions in HOIPs, compared with their inorganic counterparts. Moreover, the A-site organic ammoniums can be polar (i.e. MA, DMA), and their specific alignments, which are often induced *via* hydrogen-bonding with the perovskite framework may give rise to bulk electric ordering[37]. Such ferroelectric or antiferroelectric ordering is consequently dependent on the hydrogen-bonding strength and the dipole moments of the A-site cations as we shall discuss in detail below.

Many important properties of perovskites, such as ferroelectricity, magnetism and multiferroicity, arise due to the occurrence of phase transitions[38]. The cooperative behaviour of the A, B and X-sites across phase transitions in HOIPs give rise to many new functionalities that pure inorganics are unable to show. In particular, hydrogen-bonding has been shown to play a substantial role in creating ferroic[39] and multiferroic[40] properties, and modulating the conductivity[41] as well as the dielectric[42] properties of HOIPs. Apart from the interesting properties associated with phase transitions, HOIPs have also been found to show other novel properties beyond inorganic ones. The hybrid perovskite halides exhibit impressive photovoltaic performance and striking light emitting properties[43]; the formate perovskites show tuneable mechanical properties[44]; and the dicyanamide perovskites display extraordinary thermal expansion[45]. These different hybrid perovskite classes will now be discussed in more detail.

Hybrid halide perovskites

Discovery and structures of hybrid metal-halides. Solar cell technology requires materials with high efficiencies, simple processability, low cost and abundant availability from Earth. The particular class of *hybrid metal-halide* perovskites, offers vast opportunities to integrate all the above requirements[46]. As there are several review papers concerning the use of halide HOIPs in solar cells[43, 46-50], we only discuss their history briefly herein. The very first halide HOIPs, $MAPbX_3$ (X = Cl, Br, I) were synthesised and structurally characterised by Weber in 1978[9, 51] although it has been suggested that the halide HOIPs might already have been prepared in the early 1880s[52]. About a decade after Weber's work, Mitzi and co-workers carried out systematic research on the

synthesis, characterisations and properties of these solar cell HOIPs, pioneering the study of HOIPs as optoelectronic materials[54-56]. In 2009, the first study using halide HOIPs in a dye-sensitised photovoltaic device architecture was published by Miyasaka and co-workers, in which they reported that the self-organisation potential of $MAPbBr_3$ sensitizer in mesoporous TiO_2 gave solar cells with a light-to-electricity conversion efficiency of about 3.8%[57]. Following this pioneering work, the groups of Snaith at Oxford and Grätzel at the École Polytechnique Fédérale de Lausanne fabricated solar cells with ~9% efficiency using a dye-sensitised architecture in 2012[58, 59]. In the following year, Snaith and co-workers reported the first planar device architecture with an efficiency of about 15% using the $MAPbI_3$ layer solely as the light-absorber and active layer[60]. This work confirmed the key functionality of the HOIP as both an absorber and charge-generating layer, and also simplified the device design by excluding the TiO_2 scaffolding. The latest progress has pushed the potential conversion efficiency in a tandem configuration with a silicon cell to over 25% for small cells using a mixed-cation lead mixed-halide perovskite absorber[61], which is approaching the efficiencies of the best single-junction GaAs cells which have an efficiency of about 29% (but after nearly 60 years of development)[62].

Despite their huge impact on photovoltaics and other applications, only a handful of solar cell HOIPs with advantageous properties for use in optoelectronic applications have been discovered thus far[46]. The B-site is limited to the IVA group metals, lead and tin, with divalent charge, and the X-site is chosen from three different halides – Cl^-, Br^- and I^-. The resulting BX_3^- frameworks can thus only accommodate the smallest organic cations such as MA and FA (FA = formamidinium) according to the Goldschmidt

tolerance factors[19]. Larger moieties at the A-site lead to layered structures, which tend to exhibit limited bulk charge transport[53].

The reported photovoltaic HOIPs, as tabulated in Table 1, have been demonstrated to undergo successive phase transitions with temperature perturbation, many of them first order, evolving from cubic to tetragonal, then to orthorhombic symmetry upon cooling[56, 63]. Since the free MA and FA cations do not have the symmetry required for the cubic and tetragonal phases, they often have to be orientationally disordered to stabilize those particular symmetries[64, 65]. The rotation of the A–site organic amine cations is more restricted in the lowest temperature phases of each compound, rotating only around the C–N axis, if at all[66]. The MA and FA cations are interacting with the perovskite framework *via* N–H•••I hydrogen bonding, in addition to electrostatic force, in marked contrast to their oxide counterparts, which consequently affects their phase transitions, along with octahedral tilting and disorder[67]. In addition, the different hydrogen bonding modes of MA and FA cations lead to divergence of their interactions with the anionic framework and consequently to distinctive phase transition mechanisms and dynamics[68].

Concerns have been raised about the toxicity of lead and tin HOIPs and the connected potential limitations on their widescale use in solar energy technology[69]. A more severe limitation could be posed by instability under atmospheric conditions, in particular humidity, and the unclear effect of phase transitions at elevated temperatures on photovoltaic performance. These issues can be partially addressed by device encapsulation, which is an established technique for commercial photovoltaics[70].

Nevertheless, a search for more stable and eco-friendly photovoltaic HOIP materials has started to emerge. Recently, mixed cation perovskite films[61] and 2D layered

perovskites[71] have been put forward as materials for devices with increased stability. Thorough investigations of the fundamental properties of these new systems and testing of such devices for extended times is required to fully secure their future use in commercial applications. In particular, instability under illumination has been observed in systems with mixed-halide compositions[72]. Replacing Pb/Sn by Ge, a family of new solar cell HOIPs have been successfully prepared, which include $MAGeI_3$, $FAGeI_3$ and $[ACA][GeI_3]$ (ACA = acetamidinium)[73]. These materials have bandgaps of ~1.6–2.2 eV, which could enable them as possible photovoltaic materials though the instability of Ge^{2+} is also an issue.

Another possible approach is to substitute Pb/Sn/Ge divalent metals by a combination of monovalent and trivalent metals to construct double perovskites. This has been realised in two inorganics ($Cs_2AgBiCl_6$ and $Cs_2AgBiBr_6$)[74-76] and a hybrid ($[(MA)_2][KBiCl_6]$)[26], with indirect bandgaps between ~2.2–3.0 eV[26]. These new halide HOIPs with eco-friendly compositions exhibit good thermal, moisture and mechanical stability, indicating a quite promising direction towards material optimisation though the bandgaps still need to be further lowered. A very recent experimental breakthrough, guided by first principles calculations, revealed the successful preparation of another double perovskite, $(MA)_2TlBiBr_6$, which is isoelectronic with $MAPbBr_3$ and shows very similar optical behaviour with a direct bandgap of ~2.0 eV[26]. Though the toxicity of thallium is even more disadvantageous than that of lead, employment of other benign monovalent metals such as Cu^+ and Ag^+ is predicted to give rise to comparable bandgaps to lead HOIPs, according to calculations using density functional theory.

Physical Properties. The good solar cell performance of the halide HOIPs originates from their superior semiconducting properties. They are direct bandgap semiconductors, with experimentally observed bandgaps in the range from ~1.2 to ~3.1 eV (Figure 3a). Their bandgaps are predominantly determined by the halogens due to the strong contribution of the halogen *p*-orbitals to the optical transition, but they can also be fine-tuned by varying the B-site metal. However, the bandgaps are only weakly dependent on the A-site organic cations due to their relatively weak electronic interactions with the anionic framework. Iodides are most suitable for photovoltaic applications since their bandgaps (~1.2 to ~1.6 eV) are in the vicinity of the optimal value of ~1.1 to ~1.5 eV for a single junction photovoltaic devices under the standard solar spectrum according to the Shockley–Queisser model[77]. To understand the fundamental electronic structure of these halides in a simple way, we take the cubic phase of $MAPbI_3$, which is easier in terms of computational efforts compared with the ambient tetragonal phase, to exemplify the electronic structure through recent theoretical studies[78]. As seen from Figure 3b, the valence band maximum (VBM) is mainly constructed from the 5*p*-states of I, mixed with a certain percentage of the 6*s*-orbitals of Pb, while the conduction band minimum (CBM) originates primarily from the 6*p*-states of Pb, hybridized with a small amount of 5*p*-states of I[78]. By taking into account the spin-orbit coupling of Pb, the calculated bandgap of the cubic $MAPbI_3$ is close to the experimental value. Replacing Pb in $MAPbI_3$ with Ge, the far more distorted GeI_6 octahedra result in a much higher bandgap of ~1.9 eV[73]; and substituting Pb^{2+} by K^+ and Bi^{3+}, the low lying energy states of ionic K^+ enlarges the bandgap to be about 3.0 eV[26]. However, the coexistence of Tl^+ and Bi^{3+} on the B-site in $MATlBiBr_6$ gives rise to a bandgap (~2.0 eV) nearly identical to its Pb counterpart which

is attributed to significant contributions to both the VBM and CBM from the 6s and 6p orbitals of both metals on the B-site[26].

The properties of the crystal structure additionally affect the electronic properties, in particular the transport properties, through carrier-phonon scattering. First reports on hot carrier scattering[79, 80] and emission broadening[81, 82] as well as and calculations[83-85], suggest that carrier-phonon scattering rates in the perovskites are reduced compared to classical inorganic semiconductors. The response of the crystal lattice to the presence of non-equilibrium charge carriers populations is still under investigation, although a strong coupling between carriers and phonons has been hypothesised[86, 87]. Recent reports on calculations using the Bethe-Salpeter method suggest that electrons and holes separate after light excitation to form polarons[88]. Nevertheless, more evidence is required to address the proposition of localized charge carriers (polaron formation[84, 85]), particularly in light of the good transport values and long recombination lifetimes.

Generally, for efficient photovoltaic devices, high absorption cross sections for efficient light collection, efficient long-range charge separation, and low-loss charge transport and collection are required. The light absorption coefficients (~10^5 cm^{-1}) of solar cell HOIPs are among the highest for materials with solar cell conversion efficiency over 10%, which significantly reduces the required thickness of absorber layer to hundreds of nanometres[89]. Unexpectedly, these solution-processed materials also demonstrate high radiative efficiencies−above 50% in polycrystalline thin films[90] and 90% in nano-crystalline form[91]. Such high radiative efficiencies are usually attributed to the interaction of charge carriers with low defect densities or the fast trapping-detrapping of carriers into shallow trap states energetically close to the band. Explanations for the

low apparent defect densities are potentially related to the low temperature processing of the material and have been attributed to the flexibility of the perovskite A-site, which allows spatial adjustment during fabrication, so that stress in the lattice can be released and pure crystals can form more easily, driving structural defects out. Defect tolerance can also be achieved by partially oxidized post-transition metals[92] or defect self-healing[46]. A better understanding is required of the nature of the defect states; hitherto, this, has been mainly addressed by theoretical calculations[93, 94] and photoelectron spectroscopy in high vacuum[95-99]. While high crystal lattice order has been reported from diffraction measurements on poly-crystalline films, more evidence is needed on the actual size of the single-crystalline domains in these films, which might be very different from the grain boundaries observed in microscopy, and their role in defect formation. Importantly, future work needs to provide a clear distinction between the effects of defect states and the effects of potential polaron formation on charge carrier recombination.

The solar cell HOIPs also display long diffusion lengths beyond 100 nm for both holes and electrons[100]. The long carrier lifetimes, in combination with high radiative efficiencies, require a consideration of photon recycling when discussing carrier transport in thin films under illumination. It has been recently reported, that initially photoexcited carriers can recombine at distances away from the excitation spot to re-generate photons, which then can be reabsorbed to form charge carriers at significant distances away from the initial excitation point[101]. The long transport lengths suggest that these materials can function effectively in a thin–film architecture, since charges can be transported in the perovskite over long distances. The exciton binding energy (E_B), which defines the lowest energy required to dissociate an exciton (electron–hole pair), must be small in

order to achieve efficient charge–carrier separation. Experimental reports agree with the picture that photoexcitations in the HOIPs directly form free electrons and holes, rather

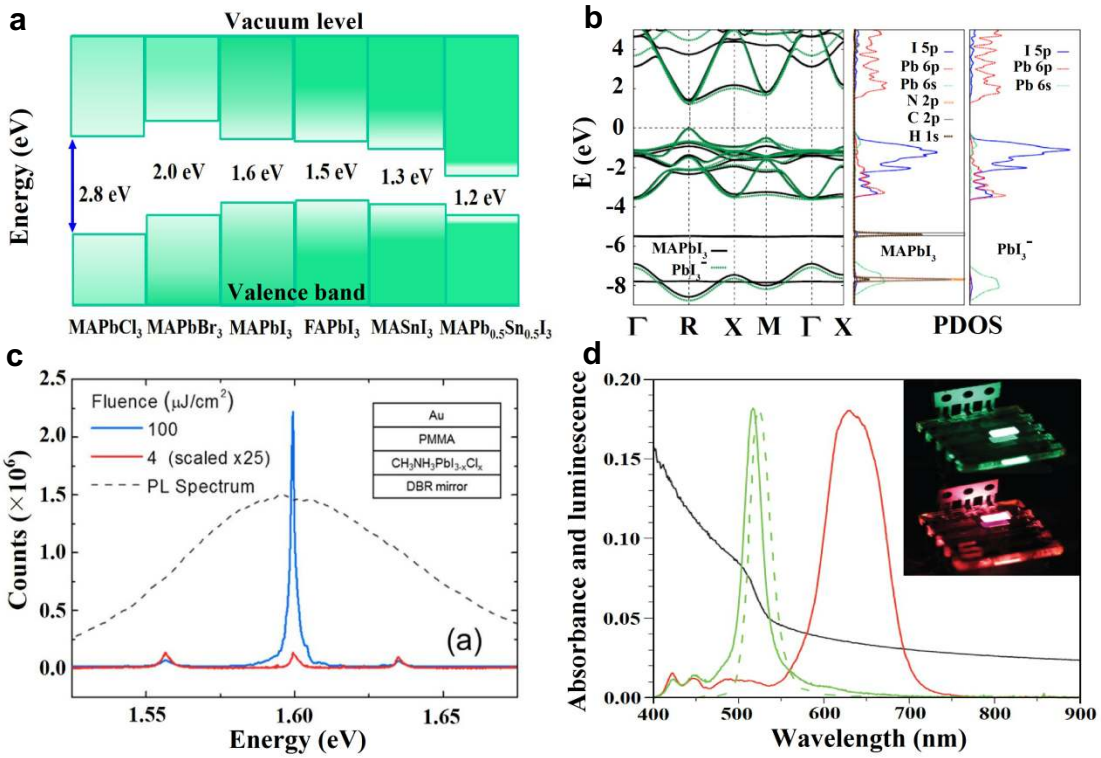

Figure 3 | **Semiconducting, lasing and LED properties of solar cell HOIPs.** a | Energy levels (in eV) for different solar cell HOIPs (REF. 54). b | Bandgap structures and the projected density of states of the cubic inorganic framework PbI_3^- and the unrelaxed cubic $MAPbI_3$ (with the organic molecule along the [001] direction), calculated using the Perdew-Burke-Ernzerhof functional within the DFT framework (REF. [78]). Green and black depict the calculation results of the PbI_3^- and $MAPbI_3$, respectively. It is clear that MA cation contributes very little to the band-edge states. c | Emission spectra of a vertical microcavity from the gain medium of a 500 nm $MAPbI_{3-x}Cl_x$ film in the laser device shown in the inset (REF. [90]). The HOIP film was excited using a 0.4 ns pulsed laser at 2.33 eV, and 4 and 100 μJ/cm^2 fluences. The mode at 1.6 eV is amplified when the excitation is above the lasing threshold of ~0.2 μJ pulse energy. DBR: distributed Bragg reflector. d | Absorption (black line), photoluminescence (dashed green line) and electroluminscence (solid green line) spectra of the $MAPbBr_3$ perovskite nano-films (REF. [107]). The normalized EL spectrum of the $MAPbBr_2I$ perovskite is also shown in red, which indicates the emissions are colour-tuneable. Image b reprinted with permission from REF.[78], American Physical Society. Images c and d reprinted with permission from REFs. [90, 107], Nature Publishing Group.

than bound excitons, since the E_B is low enough to enable charge separation at room temperature, i.e. ≤ 25meV[102-105]. Furthermore, the electron–hole effective masses of HOIPs[86], which are close to those of prototypical inorganic semiconductors such as GaAs[106], indicate good transport performance. The above attributes are requirements of an optimal material for a single-junction solar cell and contribute to the high efficiencies of the HOIP–based solar cells.

Materials with good performance for converting light to electricity can also be excellent electrically driven light emitters[108]. In this context, the outstanding long carrier lifetimes and low non-radiative recombination rates of solar cell HOIPs are enabling attributes for lasing structures. Friend and co-workers successfully constructed a HOIP-based microcavity structure by simply sandwiching the $MAPbI_{3-x}Cl_x$ emitter between two reflective layers (Figure 3c)[90]. By downscaling of the resonator structures to the nanoscale, $MAPbX_3$–based nanowire lasers with reduced lasing thresholds were fabricated[109], possibly due to the higher Q-factor and single-crystalline nature of the nanostructures. More importantly, the emitting wavelength can be readily tuned to cover the whole visible light range *via* the simple alteration of the X-site[110]. Further work shows that near-infrared lasing has been successfully realized in planar nanopores which is of vital importance to identify random from spatially coherent lasing[111, 112]. Recent developments used surfactant micelles as soft templates to control the growth of $MAPbBr_3$ micro-structures from 1D microwires to 2D microplates. The former emits strong green light with intense spots at the ends while the latter gives bright emissions at the rectangular edges but very weak emissions from the bodies[113]. The demonstration of low-threshold lasing in macroscopic feedback structures will be crucial for future

development of perovskite laser structures.

The broadband colour tunability and high photoluminescence quantum efficiencies of perovskite halides also make them promising materials for uses in low-cost and large-area light-emitting diode (LED) devices. The bulk HOIP based LEDs, demonstrated by Friend and co-workers in simple multilayered devices, emit near-infrared, green and red light at room temperature, depending on the type and quantity of halides in the HOIP emitters (Figure 3d)[107]. Their bright electroluminscence benefits from the efficient radiative recombination of injected electrons and holes[114]. However, the efficiencies of these LEDs are lower compared to conventional organic and quantum-dot ones, probably due to the poor morphology of the HOIP thin layers[114]. A follow up from the Cambridge group demonstrated improved LED performance by embedding nanocrystalline HOIPs into a pinhole-free matrix of dielectric polymer with improved morphology and higher efficiency[114]. Recently, uniform $MAPbBr_3$ nanoplatelets with very high crystallinity, prepared through a facile solution method, were used to fabricate LEDs. The resulting devices emit bright, stable and spectrally narrow 529 nm green light, with remarkably high yield of over 85%[115]. In addition, the superior resistance to moisture of these LEDs avoids the use of glove-box preparation, thus leading to a new avenue for the cheap and scalable processing that is required by industry.

The polar nature and order-disorder transitions of MA and FA cations across phase transitions in halide HOIPs bring the question as to whether they can align in an ordered way to give rise to ferroelectricity. The existence of ferroelectric domains in the crystal lattices will aid in the enhancement of electron-hole separation, and consequent higher photovoltaic performance[46]. Stoumpos *et al.* reported the first possible evidence of the

ferroelectric properties of $MAPbI_3$ in the ambient tetragonal phase by observing a hysteresis in the current-voltage plots[73]. Then, Kutes *et al.* claimed the first direct experimental evidence of ferroelectric domains using piezoelectric force microscopy[116]. The complex atomic origins were elaborated by Stroppa *et al.* and others utilising DFT calculations and symmetry mode analysis, and the spontaneous polarisation was found from the combined contributions of the relative movement of MA and the relaxation of the framework, which are coupled by hydrogen-bonding[117-119]. However, further experimental work on the $MAPbI_3$ thin films using impedence spectroscopy disagrees with the above conclusions[120] and more solid experimental evidence is highly needed in order to validate the aforementioned theoretical results.

Considering the large spin-orbital coupling (SOC) inherently carried by Pb and Sn metals and the possible asymmetry in these halides, one might wonder whether these two phenomena can couple with each other to generate the Rashba effect. Kim *et al.* researched the tetragonal phase of $MAPbI_3$, which is possibly ferroelectric using density functional theory, and found that the helical direction of the angular momentum texture in the Rashba band can be tuned *via* ferroelectric switching[121]. Further work led by Stroppa *et al.* about another possible ferroelectric $FASnI_3$, demonstrates that the relatively strong SOC in this asymmetric HOIP results in a co-existence of the Rashba and Dresselhaus effects and to a spin texture which is able to be induced, tuned and switched by external electric fields *via* controlling the ferroelectric state[122]. As the ferroelectricity in these two materials is strongly related to the configurations of the polar A-sites, the above work highlights the intriguing interplay between the SOC and organic dipole ordering which have not been seen in traditional spintronic materials.

Mechanical properties of perovskite halides are critical as they influence the manufacturing and processing significantly[123, 124]. Cheetham and co-workers utilised nanoindentation techniques to probe the fundamental elastic and plastic properties of $MAPbX_3$ (X = Cl, Br and I) single crystals[125]. The measured Young's moduli, which lie in the range ~10–20 GPa, correlate well with the structural and chemical differences in these analogues, where framework stiffness varies with Pb–X bond strength, tolerance factor, as well as the electronegativity of the halogen atoms. However, the hardness properties show an inverse trend, giving the best–performing solar $MAPbI_3$ the highest hardness. Latter work by Cohen and colleagues reported consistent results, and also analysed the thermal expansion behaviour of these halides[126]. Their pronounced thermoelastic response (~30–40 $\cdot$ 10^{-6} $\cdot$ K^{-1}), due to the octahedral flexing, might lead to ductility and flexibility which could facilitate the 'self-healing' of point defects during device operation. In contrast, the relatively low hardness properties indicate ease of plastic deformation, which could affect the cyclability of flexible cells and devices.

Hydrostatic deformation occurs along with uniaxial stressing in any manufacturing processes, therefore the high-pressure behaviour of the perovskite halides has also been explored[124, 127]. Wang and co-workers examined the hydrostatic behaviour of $MAPbBr_3$ in great detail, and found the occurrence of successive phase transitions at ~0.4 and ~1.1 GPa pressure[128]. Very recently, Zou and Mao claimed that $MAPbI_3$ can experience a tetragonal to orthorhombic phase transition at an even lower pressure of about 0.3 GPa[129, 130]. Such pronounced transitions involve significant structural and bonding alternations, and corresponding bandgap changes[130]. As flexible devices are the future trend, solar cell performance which could be influenced by phase transitions during significant device

bending will be a critical issue that must be taken into account. In addition, the sensitivity to compression of these halides also indicates some metastable phases might be synthesized under medium pressure.

Hybrid formate perovskites

Synthesis and chemical diversity. The limited size of halogen atoms only enables the construction of perovskites using smaller A-site cations such as MA and FA, so larger and longer A-site organic cations cannot be accommodated unless the X–site linkers are extended according to the aforementioned Goldschmidt tolerance factors. The formate group ($HCOO^-$) is a bridging and monovalent linker with an effective length of about 4.5 Å[19], which enables it to function as an ideal replacement for halogens to accommodate a wide range of organic amine cations. Accordingly, perovskite–like metal–formate frameworks have been synthesized using this strategy under mild solution conditions[131]. By using various protonated amine cations (from the smallest, ammonium, to the largest, TMA) and six-coordinated divalent metals, about 45 different formate-based perovskites have been discovered, making them the largest family of hybrid perovskites (Table 1)[12, 22-24, 42, 132-145]. The formate linker adopts an *anti-anti* coordination mode in most cases (but *anti-syn* in a few compounds[22-24, 34]) and bridges adjacent metals to form cubic or pseudocubic cavities in which the amine cations, with effective radii from 1.46 to 2.92 Å, are located[12, 136]. Changing the divalent metals for a combination of mono- and trivalent ones (i.e. Na^+ and Fe^{3+}) gives rise to a subclass of formates possessing double perovskite structures[7, 17].

Although the perovskite architecture is adopted for all these formates, the crystal

symmetries and guest-host interactions are dependent on the size, shape and nature of organic cations, leading to abundant and tuneable physical properties that we discuss below. In general, the A-site organic cations and formate linkers, with lower symmetries compared with the spherical metal ions in oxides, assemble into architectures with monoclinic, orthorhombic and trigonal space groups, and rarely in tetragonal or cubic ones for their ambient phases[7, 12, 17, 22-24, 42, 132-145]. It is noteworthy that there are abundant hydrogen-bonds in these formate HOIPs, for which the amine hydrogens on the A-site organic cations function as hydrogen donors and the oxygen atoms in the formate ligands act as acceptors. Interestingly, the hydrogen-bonding modes and strengths can be tuned by selecting organic amines with different symmetries and bonding sites. Most importantly, the A-site organics are disordered at high temperatures but usually become ordered upon cooling[7, 12, 42, 137-140]. This results in a variety of intriguing phase transitions including ferroelectric, ferroelastic and ferromagnetic cases[147, 148].

Properties. Magnetism was the first property to be explored in the formate perovskites, and their magneto-structural relationships have been extensively investigated and established by Gao, Wang and co-workers[147, 148]. Since the long distance spanned by the formate linker can only mediate weak magnetic coupling, formate HOIPs only exhibit long-range magnetic ordering below 50 K, making them less attractive in terms of practical applications. The tilting of the adjacent MO_6 octahedra bridged by the *anti-anti* formate linkers lead to noncentrosymmetric exchange pathways, which permit the occurrence of Dzyaloshinsky–Moriya interactions and result in spin-canted antiferromagnetism and weak ferromagnetism[147]. In addition, interesting hidden spin-

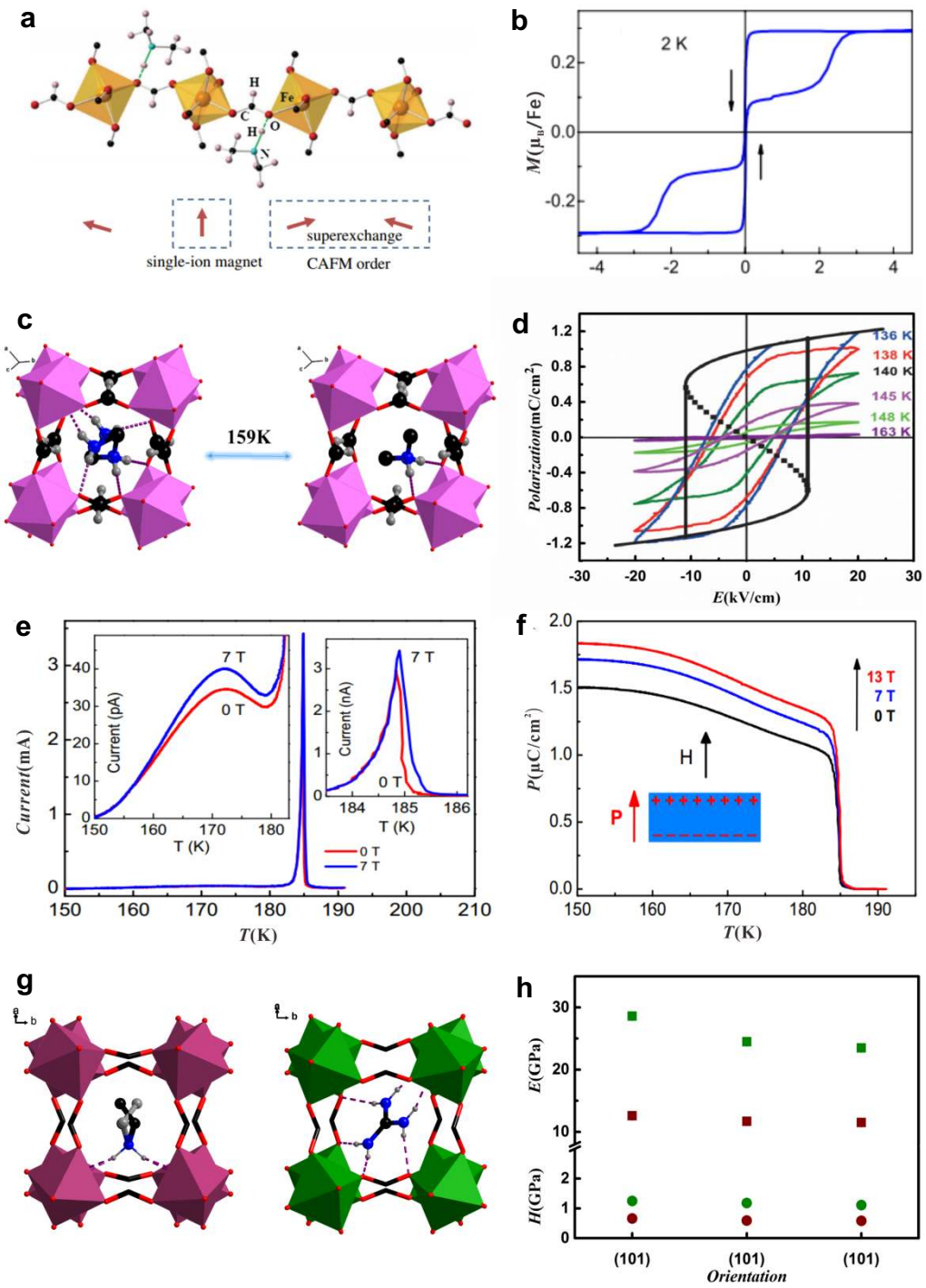

Figure 4 | **Physical properties of formate HOIPs.** a,b | Coexistence of long-range canted antiferromagnetic (CAFM) order and isolated single-ion quantum magnetism (SIQM) in [DMA][Fe(HCOO)$_3$] (REF.[150]). As shown in a, the CAFM order originates from the superexchange interactions between adjacent Fe^{2+}, and the isolated SIQM appears when the superexchange coupling is broken due to the N-H•••O hydrogen-bonding between the formate group and DMA cation. The magnetisation-field (*M-H*) hysteresis loops show

step-shaped characteristics, indicating the occurrence of resonant quantum tunnelling magnetisation as seen in b. c,d | Ferroelectric phase transition of $[(CD_3)_2ND_2][Co(DCOO)_3]$ (REF.[151]). The transition, shown in c, is mainly triggered by the order-disorder of the DAM cation and associated hydrogen-bonding variations at about 159 K. The polarisation-field (*P*-*E*) hysteresis loops collected below *Tc* with a fixed frequency at 50 Hz are displayed in d. The black line represents the fitting by the Landau theory. e,f | The electric polarisation modulated *via* a magnetic field in $[DMA][Mn(HCOO)_3]$ (REF.[40]). The pyroelectric current as a function of temperature at zero and 7 T magnetic field (e). The enlarged views below and near the ferroelectric transition are shown in the insets. The electric polarisation normal to the (012) plane under 0, 7 and 13 T fields is shown in f, and both the magnetic and electric fields were applied along the same direction as seen in the inset. g,h | Mechanical properties of $[AZE][Mn(HCOO)_3]$ and $[GUA][Mn(HCOO)_3]$ (REF.[44]). g displays the framework structures of these two formates, and the Young's modulus (*E*) and hardness (*H*) values are shown in h. Colour scheme: Fe, yellow; Co, light magenta; Mn, wine/olive; O, red; N, blue/green; C, grey and black; H, light grey. Hydrogen atoms of the ethylene, methyl and some formate groups are omitted for clarity. Hydrogen bonds are represented as dotted green and purple lines. Images a and b reprinted with permission from REF.[150], American Physical Society. Image d reprinted with permission from REF.[151], Wiley-VCH. Images e and f reprinted with permission from REF.[40], Nature Publishing Group. Image g adapted from REF.[44], American Chemical Society.

canting, spin-flop, spin- flip and large spontaneous magnetisation phenomena are present in the formate HOIPs[147]. As with conventional perovskite oxides, using dimagnetic dopants, solid solutions such as $[MA][Mn_{1-x}Zn_x(HCOO)_3]$ can be tuned from long-range order to paramagnetism[149]. More interestingly, resonant quantum tunnelling of magnetization was observed in $[DMA][Fe(HCOO)_3]$, where an intrinsic magnetic phase separation occurs due to the coexistence of long-range ordered spin-canting and isolated single-ion quantum magnetism (Figure 4a-b)[150]. This unusual phenomenon arises due to the fact that the long-distance superexchange between adjacent divalent iron centres, mediated *via* the formate group, shows significant dependence on the hydrogen-bonding

geometry. These striking discoveries highlight the important role of hydrogen-bonding in giving rise to exotic properties in formate HOIPs.

Phase transitions in conventional perovskites are mainly driven by displacements of the A- and/or B-sites and the tilting of the BX_6 octahedra. However, the primary origins of structural transitions in most known formate HOIPs are from the order-disorder behaviours of the A-site organic amines (occasionally the X-site formate group is also involved)[36]. Such order-disorder and associated alternations of hydrogen-bonding give rise to spontaneous polarisation in prototypical ferroelectric materials, such as $NaNO_2$ and KH_2PO_4, and this stimulated a search for ferroelectricity in these order-disorder type formate HOIPs[152, 153]. Cheetham and co-workers were the first to investigate electrical ordering of formates and they focused on [DMA][$M(HCOO)_3$] (M = Mn^{2+}, Fe^{2+}, Co^{2+}, Ni^{2+}, Zn^{2+}), in which the DMA cation is three-fold disordered at ambient conditions but ordered at low temperature[39, 146]. Their results revealed a significant anomaly in dielectricity at about 160 K for the zinc compound, along with differing diffraction patterns obtained from the synchrotron X-ray powder data. Further heat capacity measurements confirmed the above phase transition, though the entropy change across the transition (1.1 J K^{-1} mol^{-1}) is much lower than the value expected for a three-fold order-disorder switching (9.1 J K^{-1} mol^{-1}). Motivated by this work, Señarís-Rodríguez and co-workers characterised the structure of the manganese analogue in extensive detail and showed that the transition is indeed triggered by the switching of the DMA cation from three orientations to one at about 190 K[154]. Though the symmetry change from nonpolar trigonal *R*-3*c* to polar monoclinic *Cc*, reported in this work, suggests a probable ferroelectric transition, a definitive conclusion was not been drawn at that point. Xiong

and co-workers continued this exploration by studying the deuterated cobalt compound, $[(CD_3)_2ND_2][Co(DCOO)_3]$ (Figure 4c-d)[151]. Their structural characterisation reproduced the nonpolar to polar symmetry change obtained from early work, and independent second harmonic generation measurements fully supported such results. Furthermore, dielectric hysteresis was recorded below the transition temperature at about 155 K, and the unambiguous hysteresis loops undoubtedly confirm the intrinsic ferroelectricity of this formate HOIP. The spontaneous polarization was saturated at about 1.02 μC cm^{-2}, which is more than five times that of the first prototypical hybrid ferroelectric, Rochelle's salt (0.2 μC cm^{-2})[152]. Moreover, the frequency dependent dielectric permitivities are characteristic of a Debye-like relaxation behaviour, with an activation energy (E_a) and relaxation time of 464 J mol^{-1} and $1.02 \bullet 10^{-15}$ s, respectively. This ferroelectric behaviour resembles that of the prototypical order-disorder type ferroelectrics, such as $NaNO_2$, and opens up avenues for creating new ferroelectric relaxors with perovskite architectures beyond oxides[153]. Interestingly, by replacing the divalent first-row transition metals (Mn^{2+}, Fe^{2+}, Co^{2+}, Ni^{2+} and Zn^{2+}) with alkaline earth metal, Mg^{2+}, the transition temperature can be tuned towards ambient (~270 K), making $[DMA][Mg(HCOO)_3]$ promising for future practical applications[155]. The harder Lewis acidity of the Mg^{2+} ion compared with other divalent metal ions gives the Mg–O bonds more ionic character and localizes the negative charge on the formate oxygens. As a result, the hydrogen-bonding strength between the DMA cations and the framework (N-H•••O) is strengthened, which leads to a higher critical temperature. Further theoretical work revealed another possibility of tuning ferroelectricity *via* the alteration of the A-site amine in a manganese formate, where the polarisation can be largely increased to about 6 μC cm^{-2} by changing

EA to heavier $C_2H_5PH_3^+$ [156]. Moreover, recent DFT calculations demonstrate that the ferroelectric polarisations of [GUA][$Cr(HCOO)_3$] and [EA][$Mn(HCOO)_3$] could be increased by more than 300% *via* compressive strains, which is ascribed to the high framework flexibility constructed by the bent formate linkers[157]. As with perovskite oxides, solid solution formation can be used to control the electrical properties of these formate HOIPs. The mixed A-site formates, [HAZ_xMA_{1-x}][$Mn(HCOO)_3$] (x = 1.00-0.67), have been synthesized by dispersing the nonpolar [MA][$Mn(HCOO)_3$] into the ferroelectric [HAZ][$Mn(HCOO)_3$][158]. By this means, the A-site composition and framework distortions were successively engineered, resulting in para- to ferroelectric transitions with diffuse characteristics. Moreover, the amine dynamics have recently been studied by solid state nuclear magnetic resonance (NMR) in a closely related A-site solid solution[159].

In addition to ferroelectricity, dielectricity itself is of considerable interest due to its intriguing dependence on the order-disorder transitions. The azetidinium series, [AZE][$M(HCOO)_3$] (M = Mn^{2+}, Cu^{2+} and Zn^{2+}), was found to exhibit extraordinarily large dielectric permittivities, ε', higher than 10^4 over a broad temperature range near room temperature[160, 161]. Specifically, the copper and manganese compounds show giant ε' values of greater than 10^5 and 10^6 at 1 kHz around 280 K, and a maximum $\varepsilon' > 10^6$ for the isomorphous zinc phase occurs at 270 K at a frequency of 0.1 kHz. Such colossal values have only been found in some highly polarisable, perovskite oxide relaxors[162] (e.g. $BaTiO_3$) and conjugated polymers[163] (e.g. 2-chloroanthraquinone and tetrachlorophthalic anhydride polymer). Detailed structural analysis revealed that the dynamic puckering and conformational instability of the azetidinium cation play an important role in leading to

the colossal dielectric anomalies across the phase transition. ^{1}H NMR measurements indicate that ring-puckering of the azetidinium cations dominates the spin-lattice relaxation of the high-temperature phase, and the potential energy for the transition state of the ring-puckering decreases with lowering temperature[164]. Therefore, the high susceptibility of the potential curve with respect to the electrical field could be a likely reason for the onset of these giant dielectric anomalies near room temperature.

The existence of magnetic centres on the B-sites and the order-disorder nature of the A-sites in these formate HOIPs raises the question as to whether these properties can couple with each other to generate multiferroicity[165]. Following Cheetham and co-workers' pioneering study on this topic[146], Xiong and co-workers continued the search by looking for the magnetoelelctric coupling in the deuterated formate $[(CD_3)_2ND_2][Co(DCOO)_3]$[151]. Though the material is both ferroelectric and ferromagnetic, the dielectric permittivities remain unchanged even under a 5 Tesla field. Carpenter, Cheetham and co-workers studied the non-deuterated cobalt formate by focusing on the interplay between magnetism and ferroelasticity using resonant ultrasound spectroscopy[166]. A slight elastic anomaly below the magnetic ordering temperature of about 15 K, in the form of softening, indicates the existence of weak magnetoelastic coupling, giving the first evidence of multiferroicity in these formate HOIPs.

Inspired by these observations, Sun and co-workers examined the manganese analogue, $[DMA][Mn(HCOO)_3]$, and found that the magnetic state varies at the onset of the ferroelectric phase transition (Figure 4e-f)[40]. On the other hand, the ferroelectric polarisation can be significantly enhanced by more than 20% with application of a strong

magnetic field of 13 Tesla. Though these results are still being debated[167], the authors claimed a possible origin of the magnetoelectric coupling in the paramagnetic state due to a magnetoelastic effect that modulates both the superexchange and hydrogen bonding interactions. Subsequent work by the same group revealed that cross coupling between electric and magnetic orders exists in the isostructural [DMA][$Fe(HCOO)_3$][168, 169]. And they also demonstrated that the tunnelling magnetisation can also couple with the ferroelectric ordering in this material, extending the distinct hydrogen-bonding effect to another dimension by inducing a very unusual resonant quantum magnetoelectric effect[170]. Very recently, magnetic ordering-induced ferroelectricity and corresponding multiferroic behaviour were reported in [MA][$Co(HCOO)_3$][171]. Meanwhile, significant computational efforts have been made in order to help interpret the experimental findings[156, 172, 173]. Using sophisticated first-principles calculations, Stroppa and co-workers discovered for the first time that in [GUA][$Cu(HCOO)_3$] the cooperation between the Jahn-Teller antiferro-distortions and A-site GUA cation *via* hydrogen bonding induces ferroelectricity, and this ferroelectricity can also couple with the weak ferromagnetism to give rise to magnetoelectricity[172]. This discovery is unprecedented since the non-polar structural distortions (i.e. antiferro-distotions), which are unable to break inversion symmetry in traditional inorganic perovskites, can generate switchable polarisation through dispersion interactions with the A-site in HOIPs. This hypothesis was later confirmed by convincing experimental evidence from the same group, and they also proposed an interesting resonance switching model of the Lewis structures of GUA which unpins the microscopic mechanism for the occurrence of hybrid improper ferroelectricity[174]. They continued their theoretical work by modelling another Jahn-

Teller analogue, [GUA][Cr(HCOO)$_3$], which is yet to be synthesized[173]. In this case, the rotational modes of the A-site GUA and the Jahn-Teller distortion of the Cr^{2+} metal ions are hybridized to generate ferroelectricity by coupling with the secondary nonpolar modes. In such a hybrid improper ferroelectric, the Jahn-Teller effect is mainly responsible for the interplay between electric polarisation and weak ferromagnetism.

The mechanical properties of formate HOIPs have been explored from several interesting perspectives[44, 175]. Cheetham and co-workers measured the Young's moduli of four isomorphous metal-formate perovskites, [DMA][M(HCOO)$_3$] (M = Mn, Co, Ni and Zn) using single-crystal nanoindentation techniques[175]. The resulting modulus values (~19-25 GPa) fall in the sequence of Mn/Zn < Co < Ni, which does not show any direct link with the metal cation radii. However, the cation dependent behaviour can be well explained by taking into account their different ligand-field stabilisation energies (LFSEs). The large LFSE of the nickel cation gives rise to the higher resistance to MO_6 octahedral deformation, thus leading to the stiffer nature of the framework. Another work by Cheetham and co-workers, examined the intriguing influence of hydrogen-bonding on the elastic and plastic properties of two formates, [AZE][Mn(HCOO)$_3$] and [GUA][Mn(HCOO)$_3$] (Figure 4g-h)[44]. These two HOIPs possess similar anionic frameworks but distinct modes of hydrogen-bonding between the A-site amine cations and the perovskite framework. The cross-linking hydrogen-bonding in the guanidinium compound leads to substantially stronger constraints and correspondingly higher mechanical strengths, in marked contrast to the azetidinium case. Such huge disparity results in about 100% difference in elastic modulus and hardness, as well as about 400% difference in thermal expansion. Moreover, the applied hydrostatic pressure needed to

induce the orthorhombic to monoclinic phase transition in the guanidinium framework is about two times of that in the azetidinium analogue. All these results clearly show that mechanical engineering can be conveniently achieved *via* simple modification of the hydrogen-bonding in these formate HOIPs. It must be remembered, however, that their mechanical properties are about an order of magnitude lower than perovskite oxides, which would be disadvantageous for any potential applications in industrial environments (like their low thermal stability and high moisture sensitivity).

Other hybrid perovskites.

Azide HOIPs. Another family of HOIPs can be obtained with a variety of organic amines ~~by~~ using the bitopic linear azide group (N_3^-) on the X-site (Table 1)[10, 14, 34, 176-178]. Early work in 1986 reported the synthesis and structure of [TEA][$Ca(N_3)_3$] (TEA = tetraethylammonium), which crystalizes in a monoclinic distorted perovskite architecture[10]. Subsequent work by Rojo and co-workers reported another azide HOIP, [TMA][$Mn(N_3)_3$], by using a smaller organic amine and magnetic Mn^{2+} ion; it undergoes a monoclinic to pesudocubic phase transition at about 305 K[176]. Though the end-to-end coordination mode of the azide group can usually mediate ferromagnetic interactions, this manganese compound exhibits long-range antiferromagnetic ordering at about 70 K. The relatively high magnetic ordering temperature has stimulated further efforts to design and synthesise new azide HOIPs with potential magnetic applications. Wang and co-workers engineered a series of azide compounds, [$(CH_3)_nNH_{4-n}$][$Mn(N_3)_3$] by successively increasing the size of the A-site amine cations from MA, DMA, TrMA, to TMA[34]. These four compounds show remarkable structural phase transitions near room temperature and

their transition temperatures are strongly dependent on the A-sites (Figure 5a). More strikingly, the increase of symmetry of the organic amines is translated into the thermally driven lattice changes, whereby the ambient monoclinic structures of all four compounds transform into higher symmetries in sequence from MA to TMA. In addition, the Mn-N_3-Mn magnetic coupling pathways and corresponding long-range

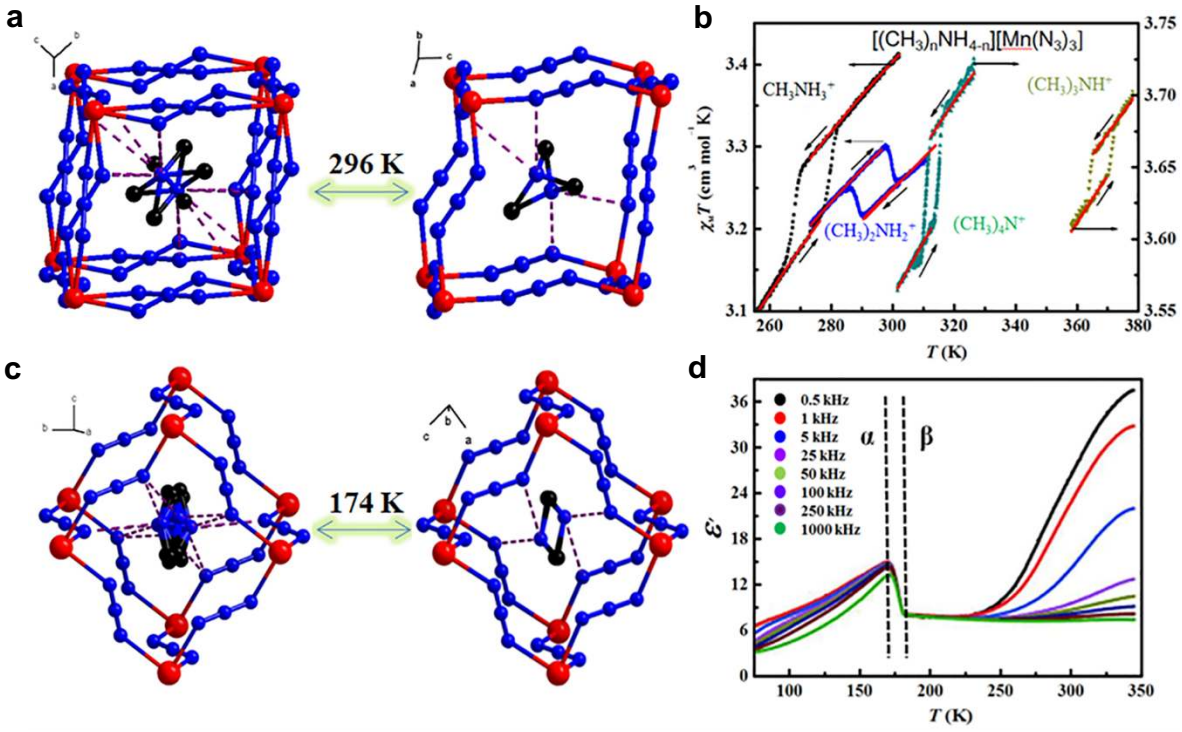

Figure 5 | **Phase transitions and associated properties of azide HOIPs.** a,b | Phase transition and magnetic bistability of [TriMA][$Mn(N_3)_3$] (REF.[34]). The symmetry breaking of the framework structure from $P2_1/c$ to $C2/c$ at about 359 K is shown in a, and the magnetic hysteresis loops are depicted in b, including [MA][$Mn(N_3)_3$], [DMA][$Mn(N_3)_3$] and [TMA][$Mn(N_3)_3$]. c,d | Ferroelastic phase transitions and associated dielectric properties of [DMA][$Cd(N_3)_3$] (REF.[178]). In c, the pseudocubic framework unit evolves from *R*-3 (β phase) to *P*-1 (α phase) at about 174 K, and in d the real part of dielectric permittivity (ε') is illustrated as a function of temperature. Colour scheme: Mn/Cd, red; N, blue; C, black. Hydrogen atoms are omitted for clarity. Hydrogen bonds are denoted as dotted purple lines. Image b adapted from REF.[34], American Chemical Society. Image d adapted with permission from REF.[178], Wiley-VCH.

ordering can also be modulated, which give rise to hysteretic magnetic bistability induced *via* structural phase transitions in a controllable manner (Figure 5b). It is worth stressing the use of symmetry induction *via* the alteration of the A-site amines in these azides since this simple and effective strategy can be readily utilised to modify other host-guest framework systems.

Zhang and co-workers extended the exploration of azide perovskites by focusing on ferrroelasticity and dielectricity[177, 178]. They first synthesized a $[TMA][Cd(N_3)_3]$ which undergoes three successive phase transitions and gives significant ferroelasticity above room temperature ($T_C \approx 320$ K)[177]. By employing size-matching bimetallic B-sites, they prepared a series of double perovskite azides, $[TMA_2][BB'(N_3)_6]$ (B = Cr^{3+} and Fe^{3+}; B' = Na^+ and K^+), which show strongly first-order phase transitions above room-temperature ($T_C \approx$ 303-320 K) associated with large entropy changes[14]. The measured dielectric permittivities are low ($\varepsilon' < 6.5$ at 100 kHz around transition) in both cases, which indicates that the non-polar TMA in the A-site needs to be replaced by a polar organic amine, in order to inject more dipoles in the crystal lattice. Very recently, they synthesised a new azide, $[DMA][Cd(N_3)_3]$, by introducing the polar DMA cation into the A-site, and the ε' of this materials is higher ($\varepsilon' \approx 15$ at 100 kHz around transition), as expected[178]. The latter HOIP undergoes a notable ferroelastic phase transition at about 175 K, which is triggered by the synergistic motion of the DMA guest and deformation of the $[Cd(N_3)_3]^-$ framework (Figure 5c). The rotational energy barrier of the guest cation shows a marked change when crossing the transition temperature upon heating, which results in a marked decrease of the dielectric permittivity, making it a possible candidate material for thermosensitive dielectrics (Figure 5d). Finally, in spite of the interesting

properties of azide HOIPs, we should note that special experimental precautions are required due to their toxic and explosive nature which, could preclude them from any possible industrial applications.

Dicyanamide HOIPs. Dicyanamide has a V-shape molecular configuration, but the long spacing between the two ends makes it a suitable bridging linker for constructing framework architectures, suggesting the possibility of creating perovskite structures. In

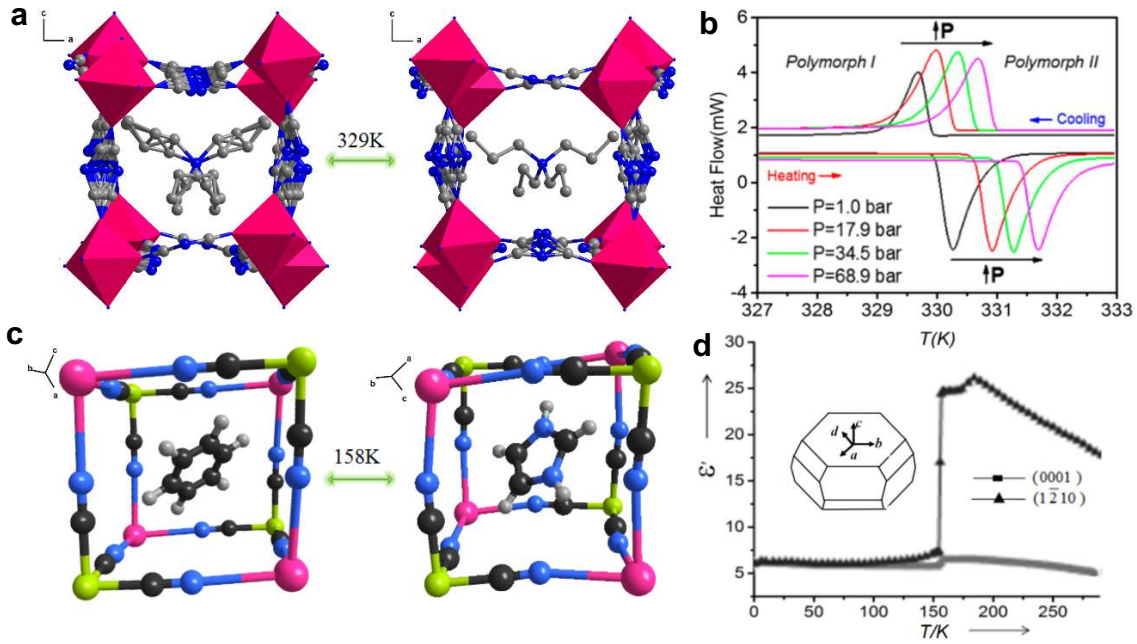

Figure 6 | **Phase transitions and corresponding properties of diacyanamide and cyanide HOIPs.** a,b | Phase transition and pressure effect of $[TPrA][Mn(DCA)_3]$ (REF.[179]). The crystal structure transforms from *I*4/*mcm* (polymorph I, right) to *P*-42$_1$*c* (polymorph II, left) at about 329 K as shown in a, and the differential scanning calorimetry curves recorded under different pressures are depicted in b. c,d | Exceptional dielectric phase transitions of $[IM]_2[KFe(CN)_6]$ (REF.[5]). The double perovskite structure switches between the high (left, *R*-3) and low temperature (*C*2/*c*) phases at about 158 K (shown in c), and in d the temperature dependent dielectric permittivity (ε') is illustrated. Colour scheme: Mn, pink; K, magenta; Fe, yellow; N, blue/Carolina blue; C, black/grey. Hydrogen atoms are omitted for clarity. Image b reprinted from REF.[179], American Chemical Society. Image d reprinted with permission from REF.[5], Wiley-VCH.

2003, Tong and co-workers reported a family of perovskite-like compounds, [BTBA][M(DCA)$_3$] and [BTEA][M(DCA)$_3$] (BTBA = benzyltributylammonium, BTEA = benzyltriethylammonium; M = Mn, Co, Fe), using dicyanamide as the X-site linker[13]. As deduced from the Goldschmidt tolerance factors, the accommodation of significantly larger A-site ammonium cations is attributed to the much longer dicyanamide linker, in marked contrast to other X-sites in HOIPs. This results in a substantially bigger pseudocubic perovskite unit cell, about three times of those of formates. Further work by Schlueter and co-workers described another family of dicyanamide HOIPs using the smaller but more isotropic tetrapropylamine, [TPrA][M(DCA)$_3$] (M = Mn and Ni)[45]. The authors focused primarily on magnetic properties, though they observed other phase transitions in these DCA compounds. Very recently, Señaris-Rodriguez and co-workers revisited these compounds and revealed the complex mechanism of the phase transition (Figure 6a)[179, 180]. Apart from the role of off-centre displacements of the TPrA cations and order−disorder of the pendant propyl groups, as well as the MN_6 octahedral tilting, order-disorder associated with the DCA bridging ligands is also involved in the complex phase transitions. The involvement of the X-site linker in phase transitions has rarely been found in other HOIPs. In addition, colossal anisotropic thermal expansion with a magnitude of 10^{-4} K^{-1} was observed for the ambient phase of the manganese compound[179]. Further high-pressure calorimetry studies also revealed that the phase transitions of the manganese and cobalt analogues are highly sensitive to external hydrostatic stimuli, with giant values of dT/dp = 242 and 184 K GPa^{-1}, respectively (Figure 6b)[180]. Such behaviour points to significant framework flexibility in these HOIPs, arising from the long DCA ligands which show a substantial response to compression.

Cyanides, dicyanometallates and borohydrides. Introducing organic components into cyano-elpasolites gives rise to another interesting subclass of HOIPs with the double perovskite structure[5, 15, 16]. An imidazolium templated cyanide, $[HIM]_2[KFe(CN)_6]$, was synthesized by Zhang, Xiong and co-workers, using potassium ferricyanide as a precursor[5]. This material undergoes two successive phase transitions at about 158 and 187 K due to the order-disorder of the A-site imidazolium (Figure 6c). As the organic cation is polar, its switching from free motion to ordered alignment induces significant anomalies in the dielectric permittivity (Figure 6d). Replacing Fe^{3+} with diamagnetic (low spin) Co^{3+}, another switchable dielectric cyanide, $[HIM]_2[KCo(CN)_6]$, was prepared, and the nature of the dynamics of imidazolium through the phase transition was established by solid-state ^1H NMR[15]. Based on the above work, the same group successfully incorporated DMA, a more polar cation compared with HIM, into the double perovskite framework. The resulting compound, $[DMA_2][KCo(CN)_6]$, shows a prominent dielectric increases at the phase transition, associated with the order-disorder behaviour of the DMA cation. Moreover, the pronounced pre-transitional fluctuations of the DMA dipoles in this HOIP lead to tuneable dielectricity over a wide temperature range, making it a promising candidate for a multifunctional molecular switch.

Extending the cyanide ligand to the linear dicyanometalate linker generates another interesting family of cyano-based HOIPs. There are 5 known dicyanometalate perovskites reported by Leznoff *et al.* and Goodwin *et al.*, respectively, including four gold-based compounds $\{PPN\}\{M[Au(CN)_2]_3\}$ (M = Mn, Co. Ni, Cd) and a silver-based one $\{PPN\}\{Cd[Ag(CN)_2]_3\}\bullet 3CH_3CH_2OH$ (PPN = bis(triphenylphosphoranylidene)ammonium)[181, 182]. The much longer $[Au(CN)_2]$ X-site

gives the largest observed pseudocubic perovskite cell with a volume of about 1000Å, which is about 4 times those in perovskite halides and the large PNN cation (~6.8 Å) is able to fit into the perovskite cavity without leading to any reduction in the framework dimensionality. Both the geometric descriptor of the tolerance factor and tilting indicator of the Glazer notation can be well exemplified in all four gold-based dicyanometallates. However, the solvated silver compound exhibits in-phase tilting of neighbouring octahedra normal to the rotation axis, which is not possible in conventional perovskites. Such features resemble those in the azide analogues[35], again highlighting the additional framework flexibility associated with the long X-sites. Moreover, the existence of intra- and inter-molecular π-π interactions involving the PNN cations introduces a new feature into the HOIP bonding.

Finally, we should mention a unique example of a perovskite-like borohydride HOIP, $[MA][Ca(BH_4)_3]$, in which the calcium metal ions and the tetrahedral BH_4^- linkers with a size of ~2.03 Å, are templated by MA[11]. The calculated tolerance factor is ~0.98, which indicates good stability for this framework with the aristotype *Pm*-3*m* symmetry. Like its inorganic analogues, this borohydride HOIP could find potential use in hydrogen storage due to the abundance of hydrogen in its crystal lattice.

Concluding comments and future perspectives

Classical oxide perovskites have played a central role in condensed matter physics and solid-state chemistry for many decades, with important examples that include titanate ferroelectrics, high temperature cuprate superconductors, magnetoresistive rare-earth manganates, and ferromagnetic metals such as strontium ruthenate. It is therefore very

exciting that an entirely new chapter of discovery has opened up with the development of hybrid perovskites. We have shown that HOIPs exhibit a great deal of chemical and structural diversity, and the range of their properties is reminiscent of classical oxide perovskites. Semiconductivity combined with excellent light-harvesting properties are found in several of the hybrid perovskite halides, and this has led to a major advance in the development of solution-processable photovoltaic devices. However, entirely new features that are absent in their inorganic analogues can be present in HOIPs, creating new properties beyond those of conventional perovskite oxides. In particular, the use of amine cations on the A-site introduces hydrogen bonding that can give rise to order-disorder transitions and provide a different mechanism for introducing electrical ordering, especially ferroelectricity. It can also lead to extremely high dielectric permittivity, which is not yet fully understood. Furthermore, the combination of such electrical ordering with magnetic ordering due to the presence of transition metal ions on the B-site has given rise to a new class of multiferroic materials. Notably, magnetoelectric coupling appears to persist well above the magnetic ordering transition, revealing another phenomenon that has yet to be fully understood.

The chemical diversity and concomitant structural variability of HOIPs offer substantial opportunities for fine-tuning their physical properties *via* facile chemical modification[183]. For example, incorporating organic components on both the A-site and X-sites confers additional functionalities and structural flexibility on the perovskite architecture, and the role of organic components in phase transitions of HOIPs, along with synergistic octahedral tilting, can lead to very complex behaviour. We hope to have shown that the well-known solar cell perovskites inhabit only a small corner of the HOIP

landscape and that the existence of formates, azides, dicyanamides, cyanides, dicyanometallates and boronhydrides illustrates the many opportunities beyond the halides.

It is interesting to consider some of the future challenges and opportunities in this exciting area. In the realm of the hybrid perovskite halides, the challenges are well-known and largely focus around toxicity (especially with lead) and chemical and thermal stability. However, these issues are being addressed, especially in terms of encapsulation and the exploration of double perovskites materials. We note that the hybrid double perovskites that have been reported to date involve chlorides and bromides, rather than iodides, offering another direction for future study. Double perovkites materials also present an opportunity to incorporate magnetic transition metal and rare-earth ions on the trivalent cation site, which could lead to very interesting magnetic and optical properties. For non-halide systems, there are challenges in terms of their relatively poor mechanical stability and their rather low magnetic ordering temperatures due to the long superexchange pathways. In terms of opportunities, other bridging X-site linkers, such as SCN^-, OCN^- and azolate, could be used to form new classes of HOIPs. Another interesting avenue would be the study of caloric effects, since the phase transitions in HOIPs are often associated with large entropy changes, about an order-of-magnitude higher than those in oxides[184, 185]. The order-disorder behaviour and framework flexibility could be easily perturbed by external fields, thus leading to large caloric effects. In a different area, the use of diamines on the A-site enables alkaline metals and other monovalent cations to occupy the B-site and merits further exploration. And beyond the 3D HOIP materials, there are hosts of lower dimensional perovskite-related systems that

have yet to be explored. In the case of the halides there has already been extensive work in this area (as is the case with oxides), but for systems involving other linkers there has been little progress to date. The marriage of inorganic and organic components, and the integration of order and dynamics[186, 187] in these hybrid perovskites, will certainly present many academic and technological opportunities in the years to come.

References:

1. Rose, G. De perowskite, fossili novo. In : De novis quibusdam fossilibus quae in Montibus Uraliis inveniuntur. 3-5 (AG Schade, Berlin, 1839).
2. Wenk, H. & Bulakh, A. Minerals : Their Constitution and Origin (NY: Cambridge University Press, New York, 2004).
3. Sasaki, S., Prewitt, C. & Bass, J. D. Orthorhombic perovskite $CaTiO_3$ and $CdTiO_3$: Structure and space group. *Acta Cryst. C* **43**, 1668-1674 (1987).
4. Weller, M. T., Weber, O. J., Henry, P. F., Di Pumpo, A. M. & Hansen, T. C. Complete structure and cation orientation in the perovskite photovoltaic methylammonium lead iodide between 100 and 352 K. *Chem. Commun.* **51**, 4180-4183 (2015).
5. Zhang, W., Cai, Y., Xiong, R., Yoshikawa, H. & Awaga, K. Exceptional dielectric phase transitions in a perovskite-type cage compound. *Angew. Chem. Int. Ed.* **49**, 6608-6610 (2010).
6. Cheetham, A. K. & Rao, C. N. Materials science : there's room in the middle. *Science* **318**, 58-59 (2007).
7. Mączka, M., Pietraszko, A., Macalik, L., Sieradzki, A., Pikul, A. & Trzmiel, J. Synthesis and order-disorder transition in a novel metal formate framework of $[(CH_3)_2NH_2][Na_{0.5}Fe_{0.5}(HCOO)_3]$. *Dalton Trans.* **43**, 17075-170854 (2014).
8. Batail, P. et al. Antiperovskite structure with ternary tetrathiafulvalenium salts: construction, distortion, and antiferromagnetic ordering. *Angew. Chem. Int. Ed. Engl.* **30**, 1498-1450 (1991).
9. Weber, D. $CH_3NH_3PbX_3$, ein Pb(II)-system mit kubischer perowskitstruktur. *Z. Naturforsch., B* **33**, 1443-1445 (1978).
10. Mautner, F. A., Krischner, H. & Kratkv, C. Preparation and structure determination of tetraethylammonium calcium azide, $[N(C_2H_5)_4]Ca(N_3)_3$. *Z. Kristallogr.* **175**, 105-110 (1986).
11. Schouwink, P. et al. Structure and properties of complex hydride perovskite materials. *Nat. Commun.* **5**, 5706 (2014).
12. Wang, Z. et al. Anionic NaCl-type frameworks of $[Mn^{II}(HCOO)_3^-]$, templated by alkylammonium, exhibit weak ferromagnetism. *Dalton Trans.* **15**, 2209-2216 (2014).
13. Tong, M. et al. Cation-templated construction of three-dimensional α-Po cubic-type $[M(dca)_3]$-networks. syntheses, structures and magnetic properties of $A[M(dca)_3]$ (dca = dicyanamide; for A = benzyltributylammonium, M = Mn^{2+}, Co^{2+}; for A = benzyltriethylammonium, M = Mn^{2+}, Fe^{2+}). *New J. Chem.* **27**, 779-782 (2003).
14. Du, Z. et al. Structural transition in the perovskite-like bimetallic azido coordination polymers : $(NMe_4)_2[B'•B''(N_3)_6]$ (B′ = Cr^{3+}, Fe^{3+}; B'' = Na^+, K^+). *Cryst. Growth Des.* **14**, 3903-3909 (2014).
15. Zhang, W. et al. Tunable and switchable dielectric constant in an amphidynamic crystal. *J. Am. Chem. Soc.* **135**, 5230-5233 (2013).
16. Zhang, X. et al. Dynamics of a caged imidazolium cation-toward understanding the order-disorder phase transition and the switchable dielectric constan. *Chem. Commun.* **51**, 4568-4571 (2015).
17. Mączka, M. et al. Synthesis and characterization of $[(CH_3)_2NH_2][Na0.5Cr0.5\ (HCOO)_3]$: a rare example of luminescent metal-organic frameworks based on Cr(III) ions. *Dalton Trans.* **44**, 6871-6879 (2015).

18. Golschmidt, V. M. Die gesetze der krystallochemie. *Die Naturwissenschaften* **21**, 477-485 (1926).
19. Kieslich, G., Sun, S. & Cheetham, A. K. Solid-state principles applied to organic-inorganic perovskites : new tricks for an old dog. *Chem. Sci.* **5**, 4712-4715 (2014).
20. Kieslich, G., Sun, S. & Cheetham, A. K. An extended tolerance factor approach for organic-inorganic perovskites. *Chem. Sci.* **6**, 3430-3433 (2015).
21. Paton, L. A. & Harrison, W. T. A. Structural diversity in non-layered hybrid perovskites of the $RMCl_3$ family. *Angew. Chem. Int. Ed.* **49**, 7684-7687 (2010).
22. Duan, Z., Wang, Z. & Gao, S. Irreversible transformation of chiral to achiral polymorph of $K[Co(HCOO)_3]$: synthesis, structures, and magnetic properties. *Dalton Trans.* **40**, 4465-4473 (2011).
23. Antsyshkina, A. S., Poraikoshits, M. A. & Ostrikova, V. N. Sterochemistry of binary formates-crystalline structures of $K_4[Co(HCOO)_6]$ and $Cs[Co(HCOO)_3]$. *Koord. Khim.* **14**, 1268-1272 (1988)..
24. Gómez-Aguirre, L. C. et al. Room-temperature polar order in $[NH_4][Cd(HCOO)_3]$ - a hybrid inorganic-organic compound with a unique perovskite architecture. *Inorg. Chem.* **54**, 2109-2116 (2015).
25. Shang, R., Chen, S., Wang, B., Wang, Z. & Gao, S. Temperature-induced irreversible phase transition from perovskite to diamond but pressure-driven back-transition in an ammonium copper formate. *Angew. Chem. Int. Ed.* **55**, 2097-2100 (2016).
26. Wei, F. et al. The synthesis, structure and electronic properties of a lead-free hybrid inorganic-organic double perovskite $(MA)_2KBiCl_6$ (MA = methylammonium). *Mater. Horiz.* **3**, 328-332 (2016).
27. Travis, W., Glover, E. N. K., Bronstein, H., Scanlon, D. O. & Palgrave, R. G. On the application of the tolerance factor to inorganic and hybrid halide perovskites: a revised system. *Chem. Sci.* **7**, 4548-4556 (2016).
28. Glazer, A. M. Simple ways of determining perovskite structures. *Acta Cryst. A* **31**, 756-762 (1975).
29. Howard, C. J. & Stokes, H. T. Group-theoretical analysis of octahedral tilting in perovskites. *Acta Cryst. B* **54**, 782-789 (1998).
30. Stokes, H. T., Kisi, E. H., Hatch, D. M. & Howard, C. J. Group-theoretical analysis of octahedral tilting in ferroelectric perovskites. *Acta Cryst. B* **58**, 934-8 (2002).
31. Glazer, A. M. The classification of tilted octahedra in perovskites. *Acta. Cryst. A* **28**, 3384-3392 (1972).
32. Woodward, P. M. Octahedral tilting in perovskites. I. geometrical considerations. *Acta. Cryst. B* **53**, 32-43 (1997).
33. Woodward, P. M. Octahedral tilting in perovskites. II. structure stabilizing forces. *Acta. Cryst. B* **53**, 44-66 (1997).
34. Zhao, X. et al. Cation-dependent magnetic ordering and room-temperature bistability in azido-bridged perovskite-type compounds. *J. Am. Chem. Soc.* **135**, 16006-16009 (2013).
35. Gómez-Aguirre, L. C. et al. Coexistence of three ferroic orders in the multiferroic compound $[(CH_3)_4N][Mn(N_3)_3]$ with perovskite-like structure. *Chem. Eur. J.* **22**, 1-9 (2016).
36. Li, W. et al. Ferroelasticity in a metal-organic framework perovskite; towards a new class of multiferroics. *Acta Mater.* **61**, 4928-4938 (2013).
37. Ptak, M. et al. Experimental and theoretical studies of structural phase transition in a novel polar perovskite-like $[C_2H_5NH_3][Na_{0.5}Fe_{0.5}(HCOO)_3]$ formate. *Dalton Trans.* **45**, 2574-2583 (2016).
38. Mats, J. & Peter, L. Handbook of Magnetism and Advanced Magnetic Materials (John Wiley & Sons, Ltd., 2007).
39. Jain, P., Dalal, N. S., Toby, B. H., Kroto, H. W. & Cheetham, A. K. Order-disorder antiferroelectric phase transition in a hybrid inorganic-organic framework with the perovskite architecture. *J. Am. Chem. Soc.* **130**, 10450-10451 (2008).
40. Wang, W. et al. Magnetoelectric coupling in the paramagnetic state of a metal-organic framework. *Sci. Rep.* **3**, 2024 (2013).
41. Sourisseau, S. et al. Reduced band gap hybrid perovskites resulting from combined hydrogen and halogen bonding at the organic-Inorganic Interface. *Chem. Mater.* **19**, 600-607 (2007).
42. Shang, R., Xu, G., Wang, Z. & Gao, S. Phase transitions, prominent dielectric anomalies, and negative thermal expansion in three high thermally stable ammonium magnesium-formate frameworks. *Chem. Eur. J.* **20**, 1146-1158 (2014).
43. Stranks, S. D. & Snaith, H. J. Metal-halide perovskites for photovoltaic and light-emitting devices. *Nature Nanotech* **10**, 391-402 (2015).
44. Li, W. et al. Mechanical tunability via hydrogen bonding in metal-organic frameworks with the perovskite architecture. *J. Am. Chem. Soc.* **136**, 7801-7804 (2014).

45. Schlueter, J. A., Manson, J. L. & Geiser, U. Structural and magnetic diversity in tetraalkylammonium salts of anionic $M[N(CN)_2]_3^-$ (M = Mn and Ni) three-dimensional coordination polymers. *Inorg. Chem.* **44**, 3194-3202 (2005).
46. Brenner, T. M., Egger, D. A., Kronik, L., Hodes, G. & Cahen, D. Hybrid organic-inorganic perovskites: low-cost semiconductors with intriguing charge-transport properties. *Nat. Rev. Mater.* **1**, 15007 (2016).
47. Green, M. A., Ho-Baillie, A. & Snaith, H. J. The emergence of perovskite solar cells. *Nature Photon.* **8**, 506-514 (2014).
48. Jung, H. S. & Park, N. G. Perovskite solar cells: from materials to devices. *Small* **11**, 10-25 (2015).
49. Berry, J. et al. Hybrid organic-inorganic perovskites (HOIPs) : opportunities and challenges. *Adv. Mater.* **27**, 5102-5112 (2015).
50. Gratzel, M. The light and shade of perovskite solar cells. *Nature Mater.* **13**, 838-842 (2014).
51. Poglitsch, A. & Weber, D. Dynamic disorder in methylammoniumtrihalogenoplumbates (II) observed by millimeter-wave spectroscopy. *J. Chem. Phys.* **87**, 6373-6378 (1987).
52. Topsoe, H. *Oversigt. K. Danske Vidensk. Selsk. Forh.* **8**, 247 (1882).

53. Mitzi, D. B. Templating and structural engineering in organic-inorganic perovskites. *Dalton Trans.* 1-12 (2001).
54. Mitzi, D. B., Feild, C. A., Schlesinger, Z. & Laibowitz, R. B. Transport, optical, and magnetic properties of the conducting halide perovskite $CH_3NH_3SnI_3$. *J. Solid State Chem.* **114**, 159-163 (1995).
55. Kagan, C. R., Mitzi, D. B. & Dimitrakopoulos, C. D. Organic-inorganic hybrid materials as semiconducting channels in thin-film fieldeffect transistors. *Science* **286**, 945-947 (1999).
56. Mitzi, D. B. Synthesis, structure, and properties of organic-inorganic perovskites and related materials. *Prog. Inorg. Chem.* **48**, 1-121 (1999).
57. Kojima, A., Teshima, K., Shirai, Y. & Miyasaka, T. Organometal halide perovskites as visible-light sensitizers for photovoltaic cells. *J. Amer. Chem. Soc.* **131**, 6050-6051 (2009).
58. Lee, M. M., Teuscher, J., Miyasaka, T., Murakami, T. N. & Snaith, H. J. Efficient hybrid solar cells based on meso-superstructured organometal halide perovskites. *Science* **338**, 643-646 (2012).
59. Kim, H. S. et al. Lead iodide perovskite sensitized all-solid-state submicron thin film mesoscopic dolar cell with efficiency exceeding 9%. *Sci. Rep.* **2**, 591 (2012).
60. Liu, M., Johnston, M. B. & Snaith, H. J. Efficient planar heterojunction perovskite solar cells by vapour deposition. *Nature* **501**, 395-398 (2013).
61. McMeekin, D. P. et al. A mixed-cation lead mixed-halide perovskite absorber for tandem solar cells. *Science* **351**, 151-155 (2016).
62. Jenny, D. A., Loferski, J. J. & Rappaport, P. Photovoltaic effect in GaAs p-n junctions and solar energy conversion. *Phys. Rev.* **101**, 1208-1209 (1956).
63. Baikie, T. et al. A combined single crystal neutron/X-ray diffraction and solid-state nuclear magnetic resonance study of the hybrid perovskites $CH_3NH_3PbX_3$ (X = I, Br and Cl). *J. Mater. Chem. A* **3**, 9298-9307 (2015).
64. Stoumpos, C. C., Malliakas, C. D. & Kanatzidis, M. G. Semiconducting tin and lead iodide perovskites with organic cations: phase transitions, high mobilities, and near-infrared photoluminescent properties. *Inorg. Chem.* **52**, 9019-9038 (2013).
65. Weller, M. T., Weber, O. J., Henry, P. F., Di Pumpo, A. M. & Hansen, T. C. Complete structure and cation orientation in the perovskite photovoltaic methylammonium lead iodide between 100 and 352 K. *Chem. Commun.* **51**, 4180-4183 (2015).
66. Lee, J. H., Bristowe, N. C., Bristowe, P. D. & Cheetham, A. K. Role of hydrogen-bonding and its interplay with octahedral tilting in $CH_3NH_3PbI_3$. *Chem. Commun.* **51**, 6434-6437 (2015).
67. Ong, K. P., Goh, T. W., Xu, Q. & Huan, A. Mechanical origin of the structural phase transition in methylammonium lead iodide $CH_3NH_3PbI_3$. *J. Phys. Chem. Lett.* **6**, 681-685 (2015).
68. Even, J., Pedesseau, L., Jancu, J. & Katan, C. DFT and k· p modelling of the phase transitions of lead and tin halide perovskites for photovoltaic cells. *Phys. Status Solidi* (*RRL*) **8**, 31-35 (2014).
69. Babayigit, A., Ethirajan, A., Muller, M. & Conings, B. Toxicity of organometal halide perovskite solar cells. *Nature Mater.* **15**, 247-251 (2016).
70. Pern, F. J. & Glick, S. H. Photothermal stability of encapsulated Si solar cells and encapsulation materials upon accelerated exposures. *Sol. Energy Mater. Sol. Cells* **61**, 153-188 (2000).

71. Tsai, H. et al. High-efficiency two-dimensional Ruddlesden – Popper perovskite solar cells. *Nature* DOI : 10.1038/nature18306 (2016).
72. Hoke, E.T. et al. Reversible photo-induced trap formation in mixed-halide hybrid perovskites for photovoltaics. *Chem. Sci.* **6**, 613-617 (2015).
73. Stoumpos, C. C. et al. Hybrid germanium iodide perovskite semiconductors: active lone pairs, structural distortions, direct and indirect energy gaps, and strong nonlinear optical properties. *J. Am. Chem. Soc.* **137**, 6804-6819 (2015).
74. Volonakis, G. et al. Lead-free halide double perovskites via heterovalent substitution of noble metals. *J. Phys. Chem. Lett.* **7**, 1254-1259 (2016).
75. Slavney, A. H., Hu, T., Lindenberg, A. M. & Karunadasa, H. I. A bismuth-halide double perovskite with long carrier recombination lifetime for photovoltaic applications. *J. Am. Chem. Soc.* **138**, 2138-2141 (2016).
76. McClure, E. T., Ball, M. R., Windl, W. & Woodward, P. M. Cs_2AgBiX_6(X = Br, Cl) : New visible light absorbing, lead-free halide perovskite semiconductors. *Chem. Mater.* **28**, 1348-1354 (2016).
77. Abou-Ras, D., Kirchartz, T. & Rau, U. Advanced characterization techniques for thin film solar cells (eds. Kirchartz, T. & Rau, U.) 3-32 (Wiley-VCH, 2011).
78. Gao, W. et al. Quasiparticle band gap of organic-inorganic hybrid perovskites : crystal structure, spin-orbit coupling, and self-energy effects. *Phys. Rev. B* **93**, 085202 (2016).
79. Wright, A.D. et al. Electron-phonon coupling in hybrid lead halide perovskites. *Nat. Commun.* **7**, 11755 (2016).
80. Wehrenfennig, C., Eperon, G. E., Johnston, M. B., Snaith, H. J. & Herz, L. M. High charge carrier mobilities and lifetimes in organolead trihalide perovskites. *Adv. Mater.* **26**, 1584-1589 (2014).
81. Kawai, H., Giorgi, G., Marini, A. & Yamashita, K. The mechanism of slow hot-hole cooling in lead-iodide perovskite: first-principles calculation on carrier lifetime from electron-phonon interaction. *Nano Lett.* **15**, 3103-3108 (2015).
82. Brivio, F., Butler, K. T., Walsh, A. & Schilfgaarde, M. V. Relativistic quasiparticle self-consistent electronic structure of hybrid halide perovskite photovoltaic absorbers. *Phys. Rev. B* **89**, 155204 (2014).
83. Filippetti, A., Mattoni, A., Caddeo, C., Saba, M. I. & Delugas, P. Low electron-polar optical phonon scattering as a fundamental aspect of carrier mobility in methylammonium lead halide $CH_3NH_3PbI_3$ perovskites. *Phys. Chem. Chem. Phys.* **18**, 15352 (2016).
84. Brenner, T. M. et al. Are mobilities in hybrid organic-inorganic halide perovskites actually "high"? *J. Phys. Chem. Lett.* **6**, 4754-4757 (2015).
85. Zhu, X. Y. & Podzorov, V. Charge carriers in hybrid organic-inorganic lead halide perovskites might be protected as large polarons. *J. Phys. Chem. Lett.* **6**, 4758-4761 (2015).
86. Price, M. B. et al. Hot-carrier cooling and photoinduced refractive index changes in organic-inorganic lead halide perovskites. *Nat. Commun.* **6**, 8420 (2015).
87. Yang, Y. et al. Observation of a hot-phonon bottleneck in lead-iodide perovskites. *Nature Photon.* **10**, 53-59 (2016).
88. Bokdam, M. et al. Role of polar phonons in the photo excited state of metal halide perovskites. *Sci. Rep.* **6**, 28618 (2016).
89. De Wolf, S. et al. Organometallic halide perovskites : sharp optical absorption edge and its relation to photovoltaic performance. *J. Phys. Chem. Lett.* **5**, 1035-1039 (2014).
90. Deschler, F. et al. High photoluminescence efficiency and optically pumped lasing in solution-processed mixed halide perovskite semiconductors. *J. Phys. Chem. Lett.* **5**, 1421-1426 (2014).
91. Protesescu, L. et al. Nanocrystals of cesium lead halide perovskites ($CsPbX_3$, X = Cl, Br, and I) : novel optoelectronic materials showing bright emission with wide color gamut. *Nano Lett.* **15**, 3692-3696 (2015).
92. Brandt, R. E., Stevanović, V., Ginley, D. S. & Buonassisi, T. Identifying defect-tolerant semiconductors with high minority-carrier lifetimes: beyond hybrid lead halide perovskites. *MRS Commun,* **5**, 265-275 (2015).
93. Yin, W., Shi, T. & Yan, Y. Unusual defect physics in $CH_3NH_3PbI_3$ perovskite solar cell absorber. *Appl. Phys. Lett.* **104**, 063903 (2014).
94. Kim, J., Lee, S., Lee, J. H. & Hong, K. The role of intrinsic defects in methylammonium lead iodide perovskite. *J. Phys. Chem. Lett.* **5**, 1312-1317 (2014).
95. Schulz, P. et al. Electronic level alignment in inverted organometal perovskite solar cells. *Adv. Mater. Interfaces* **2**, 1400532 (2015).

96. Adinolfi, V. et al. The in-gap electronic state spectrum of methylammonium lead iodide single-crystal rerovskites. *Adv. Mater.* **28**, 3406-3410 (2016).
97. Philippe, B. et al. Chemical and electronic structure characterization of lead halide perovskites and stability behavior under different exposures-a photoelectron spectroscopy investigation. *Chem. Mater.* **27**, 1720-1731 (2015).
98. Schulz, P. et al. Interface energetics in organo-metal halide perovskite-based photovoltaic cells. *Energy Environ. Sci.* **7**, 1377 (2014).
99. Lindblad, R. et al. Electronic structure of $CH_3NH_3PbX_3$ perovskites : dependence on the halide moiety. *J. Phys. Chem. C* **119**, 1818-1825 (2015).
100. Stranks, S. D. Electron-hole diffusion lengths exceeding 1 micrometer in an organometal trihalide perovskite absorber. *Science* **342**, 341-344 (2013).
101. Pazos-Outón, L. M. et al. Photon recycling in lead iodide perovskite solar cells. *Science* **351**, 1430-1433 (2016)
102. Shi, D. Low trap-state density and long carrier diffusion in organolead trihalide perovskite single crystals. *Science* **347**, 519-522 (2015).
103. Johnston, M. B. & Herz, L. M. Hybrid perovskites for photovoltaics : charge-carrier recombination, diffusion, and radiative efficiencies. *Acc. Chem. Res.* **49**, 146-154 (2016).
104. Rehman, W. et al. Charge-carrier dynamics and mobilities in formamidinium lead mixed-halide perovskites. *Adv. Mater.* **27**, 7938-7944 (2015).
105. Milot, R. L., Eperon, G. E., Snaith, H. J., Johnston, M. B. & Herz, L. M. Temperature-dependent charge-carrier dynamics in $CHNH_3PbI_3$ perovskite thin films. *Adv. Funct. Mater.* **25**, 6218-6227 (2015).
106. Nelson, R. J. & Sobers, R. G. Minority-carrier lifetimes and internal quantum efficiency of surface-free GaAs. *J. Appl. Phys.* **49**, 6103-6108 (1978).
107. Tan, Z. et al. Bright light-emitting diodes based on organometal halide perovskite. *Nature Nanotech.* **9**, 687-692 (2014).
108. Miller, O. D., Yablonovitch, E. & Kurtz, S. R. Strong internal and external luminescence as solar cells approach the shockley-queisser limit. *IEEE J. Photovolt.* **2**, 303-311 (2012).
109. Zhu, H. et al. Lead halide perovskite nanowire lasers with low lasing thresholds and high quality factors. *Nat. Mater.* **14**, 636-642 (2015).
110. Xing, G. et al. Low-temperature solution-processed wavelength-tunable perovskites for lasing. *Nature Mater.* **13**, 476-480 (2014).
111. Zhang, Q., Ha, S. T., Liu, X., Sum, T. C. & Xiong, Q. Room-temperature near-infrared high-Q perovskite whispering-gallery planar nanolasers. *Nano Lett.* **14**, 5995-6001 (2014).
112. Wiersma, D. S. The physics and applications of random lasers. *Nature Phys.* **4**, 359-367 (2008).
113. Sutherland, B. R., Hoogland, S., Adachi, M. M., Wong, C. T. O. & Sargent, E. H. Conformal organohalide perovskites enable lasing on spherical resonators. *ACS Nano* **8**, 10947-10952 (2014).
114. Li, G. et al. Efficient light-emitting diodes based on nanocrystalline perovskite in a dielectric polymer matrix. *Nano Lett.* **15**, 2640-2644 (2015).
115. Ling, Y. et al. Bright light-emitting diodes based on organometal halide perovskite nanoplatelets. *Adv. Mater.* **28**, 305-311 (2016).
116. Kutes, Y. et al. Direct observation of ferroelectric domains in solution-processed $CH_3NH_3PbI_3$ perovskite thin films. *J. Phys. Chem. Lett.* **5**, 3335-3339 (2014).
117. Stroppa, A., Quarti, C., De Angelis, F. & Picozzi, S. Ferroelectric polarization of $CH_3NH_3PbI_3$: a detailed study based on density functional theory and symmetry mode analysis. *J. Phys. Chem. Lett.* **6**, 2223-2231 (2015).
118. Frost, J. M. et al. Atomistic origins of high-performance in hybrid halide perovskite solar cells. *Nano Lett.* **14**, 2584-2590 (2014).
119. Brivio, F., Walker, A. B. & Walsh, A. Structural and electronic properties of hybrid perovskites for high-efficiency thin-film photovoltaics from first-principles. *APL Mater.* **1**, 042111 (2013).
120. Beilsten-Edmands, J., Eperon, G. E., Johnson, R. D., Snaith, H. J. & Radaelli, P. G. Non-ferroelectric nature of the conductance hysteresis in $CH_3NH_3PbI_3$ perovskite-based photovoltaic devices. *Appl. Phys. Lett.* **106**, 173502 (2015).
121. Kim, M., Im, J., Freeman, A.J., Ihm, J. & Jin, H. Switchable S = 1/2 and J = 1/2 rashba bands in ferroelectric halide perovskites. *PNAS* **111**, 6900-6904 (2014).
122. Stroppa, A. et al. Tunable ferroelectric polarization and its interplay with spin-orbit coupling in tin iodide perovskites. *Nat Commun.* **5**, 5900 (2014).

123. Feng, J. Mechanical properties of hybrid organic-inorganic $CH_3NH_3BX_3$ (B = Sn, Pb; X = Br, I) perovskites for solar cell absorbers. *APL Mater.* **2**, 081801 (2014).
124. Lee, Y., Mitzi, D. B., Barnes, P. W. & Vogt, T. Pressure-induced phase transitions and templating effect in three-dimensional organic-inorganic hybrid perovskites. *Phys. Rev. B* **68**, 020103 (2003).
125. Sun, S., Fang, Y., Kieslich, G., White, T. J. & Cheetham, A. K. Mechanical properties of organic-inorganic halide perovskites, $CH_3NH_3PbX_3$ (X=I, Br and Cl), by nanoindentation. *J. Mater. Chem. A* **3**, 18450-18455 (2015).
126. Rakita, Y., Cohen, S. R., Kedem, N. K., Hodes, G. & Cahen, D. Mechanical properties of $APbX_3$ (A = Cs or CH_3NH_3; X = I or Br) perovskite single crystals. *MRS Commun.* **5**, 623-629 (2015).
127. Swainson, I. P., Tucker, M. G., Wilson, D. J., Winkler, B. & Milman, V. Pressure response of an organic-inorganic rerovskite : methylammonium lead bromide. *Chem. Mater.* **19**, 2401-2405 (2007).
128. Wang, Y. et al. Pressure-induced phase transformation, reversible amorphization, and anomalous visible light response in organolead bromide perovskite. *J. Am. Chem. Soc.* **137**, 11144-11149 (2015).
129. Wang, K. et al. Pressure-induced reversible phase transition and amorphization of $CH_3NH_3PbI_3$ arXiv: 1509.03717[cond-mat.mtrl-sci] (2015).
130. Jaffe, A. et al. High-pressure single-crystal structures of 3D lead-halide hybrid perovskites and pressure effects on their electronic and optical properties. *ACS Cent. Sci.* **2**, 201-209 (2016).
131. Wang, Z., Hu, K., Gao, S. & Kobayashi, H. Formate-based magnetic metal-organic frameworks templated by protonated amines. *Adv. Mater.* **22**, 1526-1533 (2010).
132. Sletten, E. & Jensen, L. H. The crystal structure of dimethylammonium copper(II) formate, $NH_2(CH_3)_2[Cu(OOCH)_3]$. *Acta Cryst. B* **29**, 1752-1756 (1973).
133. Marsh, R. E. On the structure of $Zn(C_4H_8N_2O_6)$. *Acta Cryst. C* **42**, 1327-1328 (1986).
134. Nifontova, G. A., Filipenko, O. S., Astokhova, I. P. & Lavrentiev, I. P. Copper oxidation in the CCL4-amide system-synthesis and structure of $[CH_3NH_3][Cu(HCOO)_3]$. *Koord. Khim.* **16,** 218 (1990).
135. Wang, X., Gan, L., Zhang, S. & Gao, S. Perovskite-like metal formates with weak ferromagnetism and as precursors to amorphous materials. *Inorg. Chem.* **43**, 4615-4625 (2004).
136. Hu, K., Kurmoo, M., Wang, Z. & Gao, S. Metal-organic perovskites: dynthesis, dtructures, and magnetic properties of $[C(NH_2)_3][M^{II}(HCOO)_3]$ (M = Mn, Fe, Co, Ni, Cu, and Zn; $C(NH_2)_3$ = Guanidinium). *Chem. Eur. J.* **15**, 12050-12064 (2009).
137. Pato-Doldán, B. et al. Coexistence of magnetic and electrical order in the new perovskite-like $(C_3N_2H_5)[Mn(HCOO)_3]$ formate. *RSC Adv.* **3**, 22404-22411 (2013).
138. Chen, S., Shang, R., Hu, K., Wang, Z. & Gao, S. $[NH_2NH_3][M(HCOO)_3]$ (M = Mn^{2+}, Zn^{2+}, Co^{2+} and Mg^{2+}) : structural phase transitions, prominent dielectric anomalies and negative thermal expansion, and magnetic ordering. *Inorg. Chem. Front.* **1**, 83-98 (2014).
139. Mączka, M. et al. Perovskite metal formate framework of $[NH^2\text{-}CH^+\text{-}NH_2]Mn(HCOO)_3]$: phase transition, magnetic, dielectric, and phonon properties. *Inorg. Chem.* **53**, 5260-5268 (2014).
140. Ciupa, A. et al. Synthesis, crystal structure, magnetic and vibrational properties of formamidine-templated Co and Fe formates. *Polyhedron* **85**, 137-143 (2015).
141. Gao, S. & Ng, S. W. Poly[dimethylammonium [tris(tris(μ_2-formato-κ^2O:O′)cadmate(II)]]. *Acta Crystallogr. Sect. E: Struct. Rep. Online* **66**, m1599-m1599 (2010).
142. Wöhlert, S., Wriedt, M., Jess, I. & Näther, C. Polymeric potassium triformatocobalt(II). *Acta Crystallogr. Sect. E: Struct. Rep. Online* **67**, m422-m422 (2011).
143. Rossin, A. et al. Phase transitions and CO_2 adsorption properties of polymeric magnesium formate. *Cryst. Growth Des.* **8**, 3302-3308 (2008).
144. Boča, M., Svoboda, I., Renz, F. & Fuess, H. Poly[methylammonium tris(μ_2-formato-κ^2O:O′)cobalt(II)]. *Acta Crystallogr., Sect. C: Cryst. Struct. Commun.* **60**, m631-m633 (2004).
145. Mączka, M. et al. Order-disorder transition and weak ferromagnetism in the perovskite metal formate frameworks of $[(CH3)_2NH_2][M(HCOO)_3]$ and $[(CH_3)_2ND_2][M(HCOO)_3]$ (M = Ni, Mn). *Inorg. Chem.* **53**, 457-467 (2014).
146. Jain, P. et al. Multiferroic behavior associated with an order-disorder hydrogen bonding transition in metal-organic frameworks (MOFs) with the perovskite ABX_3 architecture. *J. Am. Chem. Soc.* **131**, 13625-13627 (2009).
147. Shang, R., Chen, S., Wang, Z. & Gao, S. Metal-Organic Frameworks: Functional Magnetic Materials with Formate. *Encyclopedia of Inorganic and Bioinorganic Chemistry*, 1-23. (John Wiley & Sons, Ltd., 2014).
148. Wang, X., Wang, Z. & Gao, S. Constructing magnetic molecular solids by employing three-atom

ligands as bridges. *Chem. Commun.*, 281-294 (2008).
149. Shang, R., Sun, X., Wang, Z. M. & Gao, S. Zinc-Diluted Magnetic Metal Formate Perovskites: Synthesis, Structures, and Magnetism of $[CH_3NH_3][Mn_xZn_{1-x}(HCOO)_3]$ (x=0–1). *Chem. Asian J.* **7**, 1697 (2012).
150. Tian, Y. et al. Quantum tunneling of magnetization in a metal-organic framework. *Phys. Rev. Lett.* **112**, 017202 (2014).
151. Fu, D. et al. A multiferroic perdeutero metal-organic framework. *Angew. Chem. Int. Ed.* **50**, 11947-11951 (2011).
152. Hang, T., Zhang, W., Ye, H. & Xiong, R. Metal-organic complex ferroelectrics. *Chem. Soc. Rev.* **40**, 3577-3598 (2011).
153. Zhang, W. & Xiong, R. Ferroelectric metal-organic frameworks. *Chem. Rev.* **112**, 1163-1195 (2012).
154. Sánchez-Andújar, M. et al. Characterization of the order-disorder dielectric transition in the hybrid organic-inorganic perovskite-like formate $Mn(HCOO)_3[(CH_3)_2NH_2]$. *Inorg. Chem.* **49**, 1510-1516 (2010).
155. Pato-Doldán, B. et al. Near room temperature dielectric transition in the perovskite formate framework $[(CH_3)_2NH_2][Mg(HCOO)_3]$. *Phys. Chem. Chem. Phys.* **14**, 8498-8501 (2012).
156. Di Sante, D., Stroppa, A., Jain, P. & Picozzi, S. Tuning the ferroelectric polarization in a multiferroic metal-organic framework. *J. Am. Chem. Soc.* **135**, 18126-18130 (2013).
157. Ghosh, S., Di, S. D. & Stroppa, A. Strain tuning of ferroelectric polarization in hybrid organic inorganic perovskite compounds. *J. Phys. Chem. Lett.* **6**, 4553-4559 (2015).
158. Chen, S., Shang, R., Wang, B., Wang, Z. & Gao, S. An A-site mixed-ammonium solid solution perovskite series of $[(NH_2NH_3)_x(CH_3NH_3)_{1-x}][Mn(HCOO)_3]$ (x=1.00-0.67). *Angew. Chem. Int. Ed.* **54**, 11093-11096 (2015).
159. Kieslich, G. et al. Tuneable mechanical and dynamical properties in the ferroelectric perovskite solid solution $[NH_3NH_2]_{1-x}[NH_3OH]_xZn(HCOO)_3$. *Chem. Sci.* **7**, 5108-5112 (2016).
160. Zhou, B., Imai, Y., Kobayashi, A., Wang, Z. & Kobayashi, H. Giant dielectric anomaly of a metal-organic perovskite with four-membered ring ammonium cations. *Angew. Chem. Int. Ed.* **50**, 11441-11445 (2011).
161. Imai, Y. et al. Freezing of ring-puckering molecular motion and giant dielectric anomalies in metal-organic perovskites. *Chem. Asian J.* **7**, 2786-2790 (2012).
162. von Hippel, A. Ferroelectricity, domain structure, and phase transitions of barium titanate. *Rev. Mod. Phys.* **22**, 221-237 (1950).
163. Pohl, H. A. Giant polarization in high polymers. *J. Electron. Mater.* **15**, 201-203 (1986).
164. Asaji, T. et al. Phase transition and ring-puckering motion in a metal-organic perovskite $[(CH_2)_3NH_2][Zn(HCOO)_3]$. *J. Phys. Chem. A* **116**, 12422-12428 (2012).
165. Hill, N. A. Why are there so few magnetic ferroelectrics? *J. Phys. Chem.* B **104**, 6694-6709 (2000).
166. Thomson, R. I., Jain, P., Cheetham, A. K. & Carpenter, M. A. Elastic relaxation behavior, magnetoelastic coupling, and order-disorder processes in multiferroic metal-organic frameworks. *Phys. Rev.* B **86**, 214304 (2012).
167. Abhyankar, N., Bertaina, S. & Dalal, N. S. On Mn^{2+} EPR probing of the ferroelectric transition and absence of magnetoelectric coupling in dimethylammonium manganese formate $(CH_3)_2NH_2Mn(HCOO)_3$, a metal-organic complex with the Pb-free perovskite framework. *J. Phys. Chem. C* **119**, 28143-28147 (2015).
168. Tian, Y. et al. Cross coupling between electric and magnetic orders in a multiferroic metal-organic framework. *Sci. Rep.* **4**, 6062 (2014).
169. Tian, Y. et al. Electric control of magnetism in a multiferroic metal-organic framework. *Phys Status Solidi RRL* **8**, 91-94 (2014).
170. Tian, Y. et al. Observation of resonant quantum magnetoelectric effect in a multiferroic metal-organic framework. *J. Am. Chem. Soc.* **138**, 782-785 (2016).
171. Gómez-Aguirre, L. C. et al. Magnetic ordering-induced multiferroic behavior in $[CH_3NH_3][Co(HCOO)_3]$ metal-organic framework. *J. Am. Chem. Soc.* **138**, 1122-1125 (2016).
172. Stroppa, A. et al. Electric control of magnetization and interplay between orbital ordering and ferroelectricity in a multiferroic metal-organic framework. *Angew. Chem. Int. Ed.* **50**, 5847-5850 (2011).
173. Stroppa, A., Barone, P., Jain, P., Perez-Mato, J. M. & Picozzi, S. Hybrid improper ferroelectricity in a multiferroic and magnetoelectric metal-organic framework. *Adv. Mater.* **25**, 2284-2290 (2013).
174. Tian, Y. et al. High-temperature ferroelectricity and strong magnetoelectric effects in a hybrid

organic-inorganic perovskite framework. *Phys. Status Solidi RRL* **8,** 62-67 (2015).
175. Tan, J., Jain, P. & Cheetham, A. K. Influence of ligand field stabilization energy on the elastic properties of multiferroic MOFs with the perovskite architecture. *Dalton Trans.* **41**, 3949-3952 (2012).
176. Mautner, F. A. et al. Crystal structure and spectroscopic and magnetic properties of the manganese(II) and copper(II) azido-tetramethylammonium systems. *Inorg. Chem.* **38**, 4647-4652 (1999).
177. Du, Z. et al. Above-room-temperature ferroelastic phase transition in a perovskite-like compound $[N(CH_3)_4][Cd(N_3)_3]$. *Chem. Commun.* **50**, 1989 (2014).
178. Du, Z. et al. Switchable guest molecular dynamics in a perovskite-like coordination polymer toward sensitive thermoresponsive dielectric materials. *Angew. Chem. Int. Ed.* **54**, 914-918 (2015).
179. Bermúdez-García, J. M. et al. Role of temperature and pressure on the multisensitive multiferroic dicyanamide framework $[TPrA][Mn(dca)_3]$ with perovskite-like structure. *Inorg. Chem.* **54**, 11680-11687 (2015).
180. Bermúdez-García, J. M. et al. Multiple phase and dielectric transitions on a novel multi-sensitive [TPrA][M(dca)3] (M : Fe^{2+} , $Co^{2+}$and Ni^{2+}) hybrid inorganic-organic perovskite family. *J. Mater. Chem. C* **4**, 4889-4898 (2016).
181. Hill, J. A., Thompson, A. L. & Goodwin, A. L. Dicyanometallates as model extended frameworks. *J. Am. Chem. Soc.* **138**, 5886-5896 (2016).
182. Lefebvre, J., Chartrand, D. & Leznoff, D. B. Synthesis, structure and magnetic properties of 2-D and 3-D [cation]{$M[Au(CN)^2]_3$} (M=Ni,Co) coordination polymers. *Polyhedron* **26**, 2189-2199 (2007).
183. Saparov, B. & Mitzi, D. B. Organic-inorganic perovskites: structural versatility for functional materials design. *Chem. Rev.* **116**, 4558-4596 (2016).
184. Moya, X., Kar-Narayan, S. & Mathur, N. D. Caloric materials near ferroic phase transitions. *Nature Mater.* **13**, 439-450 (2014).
185. Scott, J. F. Electrocaloric materials. *Annu. Rev. Mater. Res.* **41**, 229-240 (2011).
186. Deng, H., Olson, M. A., Stoddart, J. F. & Yaghi, O. M. Robust dynamics. *Nature Chem.* **2**, 439-443 (2010).
187. Cheetham, A. K., Bennett, T. D., Coudert, F.-X. & Goodwin, A. L. Defects and disorder in metal organic frameworks. *Dalton Trans.* **45**, 4113-4126 (2016).

Acknowledgements

The authors acknowledge funding support from the National Natural Science Foundation of China (Grant No. 61138006 and 21571072, WL) and the Ras Al Khaimah Centre for Advanced Materials (AKC).

Competing interests

The authors declare no competing interests.